Delft University of Technology

Department of Geoscience and Engineering

Bachelor thesis

Using beamforming to maximise the detection capability of Kwintsheul's seismic array

Carleyn M. den Ouden

Supervisors:

Dr. C. Weemstra

D. F. Naranjo Hernandez

Academic year 2021/2022

Delft - July 7, 2022

Summary

To run Nature's Heat geothermal operations (Kwintsheul, The Netherlands) in a safe and efficient manner, and with the support of the local population, it is important to mitigate potential hazards. A well known potential hazard related to geothermal operations is the occurrence of induced seismicity due to injection and extraction of fluids in and from the subsurface. Monitoring the subsurface allows detecting the induced seismicity due to the geothermal operations. To monitor the seismic activity around the geothermal field of Nature's Heat project, a passive seismic network was installed by Delft University of Technology, Seismoctech (Greece), and Gastreatment Services BV. This network has detected and located one single weak event on July 14, 2019.

Within this bachelor thesis, a beamforming technique is adopted to provide a framework that can be used to detect seismic events recorded by the passive seismic network. The goal is to separate coherent signals from noise and characterize the signal (e.g., estimate propagation direction). The objective of this bachelor thesis is to assess whether beamforming is capable of lowering the detection threshold, and determining the signal's apparent velocity and back azimuth, using data recorded by the Kwintsheul seismic array. For applying the beamforming technique, Kwintsheul data was implemented in a python code, originated from Remote Online Sessions for Emerging Seismologists (ROSES).

Following applying the beamforming technique, the results of the detection, and the parameter estimation of the back azimuth and apparent velocity, are given for the P-wave and S-wave, 300.96 deg. $6.43km/s$ and 315 deg. $3.31km/s$, respectively. The results of the Fisher statistics and the f-k analysis show that beamforming is capable to discriminate coherent signals from noise.

For beamforming analysis, it is necessary to have array elements that are distant from the event. As the array design is fixed, it is, therefore, necessary to eliminate data from array elements in the proximity of the event. Hence only data from array elements in the far-field is used for beamforming. This approach decreases the number of array elements, and therefore the signal to noise ratio is decreased as well. In this case, to improve the resolution of the applied beamforming technique, the array design needs to be modified, with all array elements situated in the far-field.

Contents

CHAPTER 1

Introduction

Geothermal energy is on the rise since it is a clean energy source that can cover an increasingly larger portion of the energy demand. Geothermal energy also has no carbon footprint and does not require as much space as other energy resources, like solar and wind energy (considering square meters on land per gigawatt-hour) (Brophy, 1997). During the past ten years, geothermal energy has been prioritized in the Netherlands as the horticultural sector aims to become more sustainable (EBN, Geothermie, Warmtenetwerk, & DAGO, 2018). In 2015, nine horticultural companies, that currently operate commercial greenhouses in Kwintsheul, collaboratively started with the installation of a geothermal doublet. The operation of Nature's Heat project started in 2018, with the aim to supply a geothermal-based heating system for 64 hectares of greenhouses (Naranjo, Draganov, Polychronopoulou, de Bas, & Weemstra, 2022).

Nature's Heat project consists of an operating geothermal doublet that requires injection and extraction of fluids at a depth of approximately 2400 meters. The injection and production wells are deviated wells. The geothermal well is located in Kwintsheul, the Netherlands. From a geological perspective, Kwintsheul is located in the West Netherlands Basin (WNB), which consist of inactive normal faults. The WNB is a 60-km-wide transtensional basin that, together with the Ruhr Valley Graben and the Broad Fourteens Basin, forms a failed rift system. According to the complete earthquake catalogue of the Netherlands, the WNB has no reported seismic activity (Naranjo et al., 2022). In chapter 3, figure 3.1, the location of Nature's Heat geothermal project is shown together with a map depicting known faults in the subsurface.

To run geothermal operations in a safe and efficient manner and with the support of the local population, it is important to mitigate potential hazards. A well-known potential hazard related to geothermal operations is the occurrence of induced seismicity due to the injection and extraction of fluids in and from the subsurface. Induced seismic events are due to changes in subsurface stress distributions (Naranjo et al., 2022). However, most induced events are unlikely to result in detectable ground motions at the surface. In general, the detected events are at the microseismic level with a magnitude range of -3 to 0 (Baig & Urbancic, 2010). Therefore, felt seismic-

ity, around a magnitude range of 0 to 5 (Baig & Urbancic, 2010), is considered to be unlikely to occur during geothermal operations (Brophy, 1997). Nevertheless, one should keep in mind that geothermal operations still can trigger seismic events that could represent a risk. Monitoring the subsurface allows us to detect seismicity triggered by injecting or extracting fluids into the subsurface.

To monitor the seismic activity around the geothermal field of Nature's Heat project, a passive seismic network was installed by Delft University of Technology, Seismoctech (Greece), and Gastreatment Services BV. The description of the monitoring network is introduced in chapter 3. Delft University of Technology, Seismoctech (Greece), and Gastreatment Services BV conducted an analysis of the continuous passive seismic dataset. The analysis can be divided into two different procedures: 1) event detection, which is applied to the whole data set using an energy-based algorithm, and 2) phase picking, which follows in case of the detection of an earthquake (Naranjo et al., 2022).

The network detected and located one single weak event on July 14, 2019. In the earlier referenced study, done by Naranjo et al., 2022, an iterative linearized least-squares procedure was applied to find the event location and a coarse one-dimensional velocity model of the subsurface. The estimated event's magnitude (ML) is 0.0 (duration magnitude Md 0.16), and the estimated depth of the origin is 2.46 km.

Within this bachelor thesis, I attempt to provide a framework that can be used to detect seismic events recorded by the seismic network, which were left undetected by the aforementioned energy-based algorithm. For that purpose, I adopt a beamforming technique. Sensor arrays, like the kwintsheul seismic network, allow for enhanced detection of signals within the presence of noise: the signal-to-noise ratio (SNR) improves through constructive summation across the array elements (Evers, 2008). The goal is to separate coherent signals from noise and characterize the signal (e.g., estimate propagation direction). By lowering the detection threshold, smaller seismic events can potentially be detected. This information would be useful to the operator of the Nature's Heat project, resulting in more detailed information on a potential relationship between the production and injection operations and the local seismicity.

The objective of this bachelor thesis is to assess whether beamforming is capable of lowering the detection threshold, and determining the signals apparent velocity and azimuth, using data recorded by the Kwintsheul seismic array.
Contingent on successfully meeting this objective, beamforming could be applied to the entire Kwintsheul data set in order to find seismic events that were not detected by the energy-based algorithm. Summarizing, the research question is as follows:

"*Does beamforming lead to an improved detection of the measured microseismic event found in the Kwintsheul data?*"

The remainder of this thesis is organized as follows. Chapter 2 introduces the theory underlying beamforming techniques. Chapter 3 introduces the case study of Nature's Heat geothermal reservoir, explaining both the data processing steps and listing the corresponding results. Chapter 4 forms the discussion of this thesis. Followed by a conclusion in chapter 5.

CHAPTER 2

Methodology

This chapter introduces the theory underlying beamforming techniques. Starting, in section 2.1, with the basis of signal analysis, where Fourier transforms will play a significant role. Section 2.2 will introduce a spectral analysis tool using power spectral density (PSD) as a method. With the use of PSDs, the distribution of signal frequency can be presented. Section 2.3 explains the concept and method of array processing, where the main goal is to improve the detection of a signal by using an array. Based on array processing, an array response can be estimated, which quantifies the resolution of the beamforming technique, see section 2.4. Section 2.5 introduces the actual concept of beamforming and the corresponding formulae. Within this thesis, the focus is on the frequency domain, and therefore the frequency - wave number analysis will be introduced in section 2.6. Followed by the fisher statistics in section 2.7, which is used as a measure of variance that indicates the coherence of the signals over the array.

2.1 Signal analysis - Fourier transforms

Jean Baptiste Joseph Fourier, a French mathematician, developed a basic theory underlying signal analysis in the frequency domain. He demonstrated that any periodic waveform can be represented as a sum of sine or cosine functions, defined as Fourier series, and he developed Fourier transforms (Dempster, 2001).

Fourier Transforms are used to transform signals from the time domain into the frequency domain and therefore form the basis of signal analysis. Within the frequency domain analysis, signals are quantified in terms of their component frequencies (Dempster, 2001). This will not only give important information about the event but also about the ambient seismic noise within the recordings, which both is not apparent from time-domain analysis (Dempster, 2001).

Continuous Fourier transform
A signal is built up via using cosines/sines of different frequencies, which can be varied in by weights of shifting.

The sine wave component $X(\omega)$, at angular frequency ω, of a continuous function, $x(t)$, is given by Equation 2.1. (Dempster, 2001)

$$X(\omega) = \int_{-\infty}^{\infty} x(t)[cos(i\omega t) - isin(i\omega t)]dt \tag{2.1}$$

With $\omega = 2\pi f$, and f representing the frequency. Equation 2.1 can also be written as Equation 2.2.

$$X(f) = \int_{-\infty}^{\infty} x(t)[cos(i2\pi ft) - isin(i2\pi ft)]dt \tag{2.2}$$

Note that $X(f)$ and $X(\omega)$ are complex numbers, they contain a phase and an amplitude (Dempster, 2001).

The Fourier transform of a continuous-time signal, $x(t)$, is mostly defined in the form of a complex exponential, using Euler's relationship $e^{i\theta} = cos(\theta) + isin(\theta)$. See Equation 2.3 (Dempster, 2001).

$$X(f) = \frac{1}{\sqrt{2\pi}} \int_{-\infty}^{\infty} x(t)e^{-j2\pi ft}dt \tag{2.3}$$

The reciprocal, converting back to the time-domain, is defined as the inverse Fourier transform:

$$x(t) = \frac{1}{\sqrt{2\pi}} \int_{-\infty}^{\infty} X(f)e^{j2\pi ft}df \tag{2.4}$$

(Ziemer, Tranter, & Fanning, 2011)
Both transforms in equations 2.3 and 2.4 have an additional term $1/\sqrt{2\pi}$ before the integral to restore the symmetry of the Fourier transform from the time-domain to the frequency-domain and vice versa.

Discrete Fourier transform
In practice, one computes a discrete Fourier transform (DFT). Performing transforms on data the integrals in equations 2.3 and 2.4 are therefore replaced by summations. As a result that the continuous signal $x(t)$ becomes a discrete signal x_n, in which n is an integer and the number of sampling, taken in regular sample intervals $n\Delta t$. In terms of the sample number, Equation 2.5 is periodic in k with period N, and Equation 2.6 is periodic in n with period N. The discretisation of the signal will make the Fourier transform periodic (Ziemer et al., 2011).

To derive the DFT from the continuous-time Fourier transform, the time-sampling interval is taken as $T/N = \Delta t$, where N is the total number of samples taken in a T-second interval (time window), and the frequency-sampling interval is taken as $1/T$. Equation 2.5 and 2.6 form together the final discrete-time and discrete-frequency Fourier transform pair (Ziemer et al., 2011).

$$X_k = \Delta t \sum_{n=0}^{N-1} x_n e^{-j2\pi kn/N}, k = 0, 1, \ldots, N-1 \tag{2.5}$$

$$x_n = \Delta f \frac{1}{N} \sum_{k=0}^{N-1} X_k e^{j2\pi kn/N}, n = 0, 1, \ldots, N-1 \tag{2.6}$$

Within the DFT, $X(f)$ and $x(t)$ are replaced by X_k and x_n, respectively. Because it is derived using a sampling approach, it should be clear that the sequence X_k is periodic with period N (Ziemer et al., 2011).

2.2 Power spectral Density

The power spectral density (PSD) is a method to present the distribution of signal frequency (Dempster, 2001). Compared to the DFT, a PSD is easier to interpret visually. The PSD is computed from the DFT (section 2.1).

The direct approach is a usual method to evaluate the PSD. This method is based on the fact that the energy contained in an analogue signal, x_t, is related to the magnitude of the signal squared integrated over time (Semmlow, 2012). Equation 2.7 gives the normalized energy for a signal.

$$E = \int_{-\infty}^{\infty} |x(t)|^2 dt \tag{2.7}$$

Where $x(t)$ has been written in terms of its Fourier transform.

$$\int_{-\infty}^{\infty} |x(t)|^2 dt = \int_{-\infty}^{\infty} |X(f)|^2 df \tag{2.8}$$

Equation 2.8 is referred to Parseval's theorem for Fourier transforms (Ziemer et al., 2011). Hence $|X(f)|^2$ equals the units of energy density with frequency, also known as the PSD. From the direct approach, the PSD is derived as the magnitude squared of the Fourier transform of a waveform, see Equation 2.9 (Ziemer et al., 2011).

$$PSD(f) = |X(f)|^2 \tag{2.9}$$

2.3 Array processing

Over time, seismologists have developed various methods to process seismic data. In this section, the focus will be on array processing. While using seismic arrays, one usually assumes that some form of waveform coherence exists across different, spatially-separated sensors (Arrowsmith, 2021).

Seismological arrays

Since the 1960s, seismological arrays have played an important role in global seismology (Arrowsmith, 2021). It is a seismological tool to help lower the detection threshold of (global) earthquakes and nuclear explosions. First, the purpose of seismic arrays is to detect and identify nuclear explosions. Nowadays, seismic arrays serve also as a detection tool to help identify fine-scale structures below the resolution level of global seismology in many different places on Earth (Rost & Thomas, 2002).

Seismological arrays consist of various seismometers placed at spatial discrete points. As a result that it will reduce the noise through summation of the signals (Evers, 2008). There are a variety of designs of seismic arrays. The design of a seismic array depends on the phase of interest, the Earth's structure, land access, and the differing opinions of scientists about what constitutes a good array design (Arrowsmith, 2021). Figure 2.1 shows a variety of seismic array designs by the International Monitoring System (IMS) of the Comprehensive Nuclear-Test-Ban Treaty.

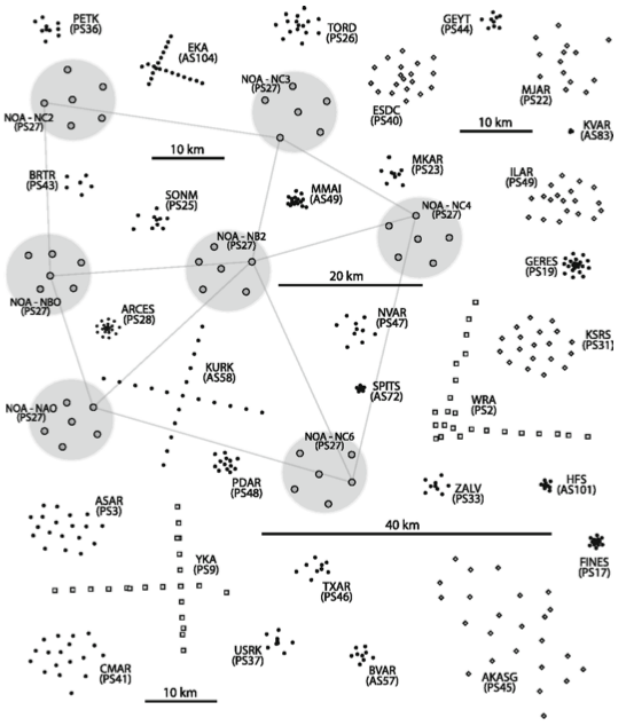

Figure 2.1: *Several designs of seismic arrays in the International Monitoring System (adopted from Arrowsmith, 2021)*

The main advantage of seismic arrays compared to single stations is that the relative size of the seismic signals is increased with respect to the ambient seismic noise. The signal-to-noise ratio (SNR) improvement is due to the summation of the individual recordings of the array stations, ideally leading to $1/\sqrt{N}$ increase in SNR, where N is the number of seismometers. This allows one to study different phases of the seismic signals (Rost & Thomas, 2002). An additional advantage of the seismic arrays is that they can determine directional information of seismic signals; it is possible to estimate the direction of propagation of the signal (Rost & Thomas, 2002).

Method

Seismic array processing assumes a plane wave arriving at the array (Rost & Thomas, 2002). The propagation direction of waves travelling in a spherical Earth and arriving at a seismological array can be described by two parameters: 1) the vertical incident angle i and 2) the back azimuth θ (figure 2.2). The amount of time for a wave to travel one meter along the Earth's surface, usually referred to as the horizontal slowness $|u|$, is described in Equation 2.10, using the vertical incident angle, ϕ, and v_{eff}, which is the medium velocity beneath the array, also known as the effective velocity (Arrowsmith, 2021).

$$|u| = \frac{sin(\phi)}{v_eff} \tag{2.10}$$

The actual slowness, u_0, can be expressed as the inverse of the effective velocity, v_{eff}. (Evers, 2008).

$$u_0 = \frac{1}{v_{eff}} \tag{2.11}$$

The effective velocity is the propagation velocity of the inclined wavefront in the xyz-space. The elements in the array measure a velocity in the xy-plane which is called the apparent velocity, v_{app}. The apparent and

effective velocities are related through the incident angle, ϕ (Evers, 2008):

$$v_{app} = \frac{v_{eff}}{cos(\phi)} \tag{2.12}$$

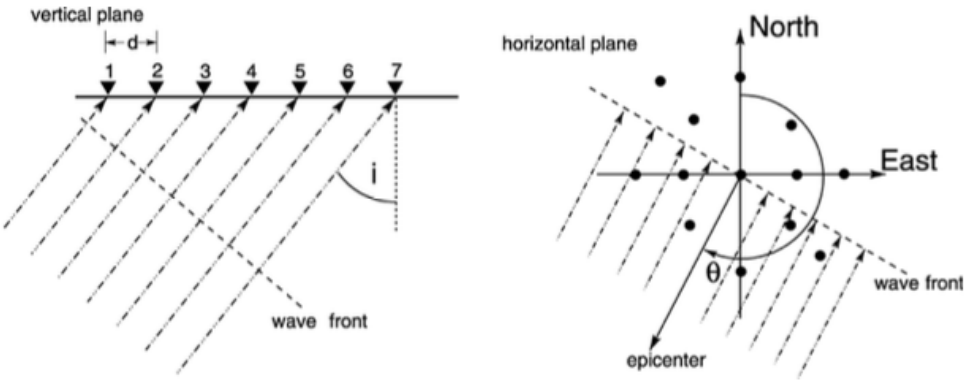

(a) (b)

Figure 2.2: (a) Vertical plane of a wave crossing the array at an incident angle i (b) Horizontal plane showing the incidental plane wave arriving with a back azimuth θ. (Adopted from Rost & Thomas, 2002)

The direction of arrival of a planar wavefront recorded on a two dimensional array can be described by the horizontal slowness vector $\vec{u} = (u_x, u_y)$ (see figure 2.3) (Arrowsmith, 2021). The horizontal slowness vector can alternatively be described in terms of 1) the back azimuth θ, and 2) its magnitude $|u|$. The vector points in the direction of horizontal wave propagation, and its modulus corresponds to the inverse of the horizontal wave speed (see Equation 2.10) (Rost & Thomas, 2002).

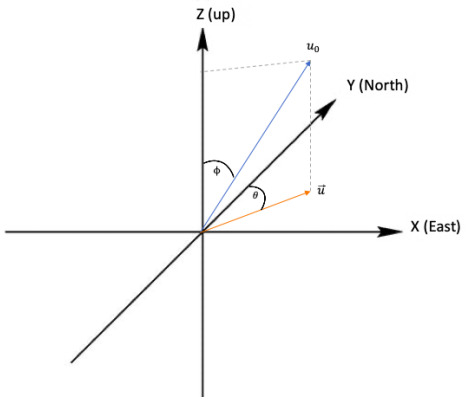

Figure 2.3: *Components of the slowness vector in the xyz-space. The slowness vector is normal to the incident wave front (adopted from Rost & Thomas, 2002)*

The apparent velocity is the horizontal propagation speed of the wavefront, i.e., $v_0/sin(i)$. And the back azimuth is the angle, measured clockwise from North, from which the plane wave arrives (e.g., the direction of an earthquake's epicenter). And can be described with the slowness vector according to Equation 2.13 (Evers,

2008).

$$\theta = tan^{-1}(\frac{u_y}{u_x}) \tag{2.13}$$

The apparent velocity is the inverse of the horizontal slowness, see equation 2.14 (Evers, 2008).

$$v_{app} = \frac{1}{|u|} \tag{2.14}$$

2.4 Array response

The array response forms the basis for an array design. Seismic arrays of seismometers discretely sample the wavefield in two dimensions. Spatial sampling is controlled by N sensors located at positions $r_j = (x_j, y_j)$, while the sample rate Δ determines the temporal sampling. Following Smart and Flinn, by Evers 2008, the array response is defined as:

$$R(f, \vec{u}) = \left| \frac{1}{N} \sum_{n=1}^{N} e^{-if[(\vec{u}-\vec{u_0})\cdot\vec{r_n}]} \right|^2 \tag{2.15}$$

With

$$\vec{u_0} = \frac{1}{f}(k_{0x}, k_{0y}) \tag{2.16}$$

$R(f, \vec{u})$ is called the beamforming array response pattern (Capon, 1969), or spatial window function (Lacoss et al., 1969) or array transfer function (Denholm-Price & Rees, 1999) (Evers, 2008).

The response pattern is calculated by assuming that the planar wave comes from right above (or below), meaning that all instruments measure the waveform at the same time. Such a waveform can be described with an apparent velocity of infinity. This infinite velocity means that there are no travel time differences over the array. The source will be located right below (or above) the array in the case of a planar wave (Evers, 2008).

In practice, the elements within an array are placed such that $R(f, \vec{u})$ in Equation 3.3 approximates a delta function around the desired slowness. The capability of detecting and classifying interfering sources relies on the beamform resolution as quantified by the array response, which is determined by the beamform technique and the array layout. A low beamform resolution could lead to the dominant source masking sub-dominant sources. A higher-resolution array, e.g., better peaked absolute maximum, can be obtained by modifying the locations of the array elements or by adding elements to the array (Evers, 2008). This can come, however, at the cost of more dominant side-lobes. Fig 2.4 shows this effect for infrasound detection, therefore $v_{app} = 340m/s$, which will not be the case in this thesis.

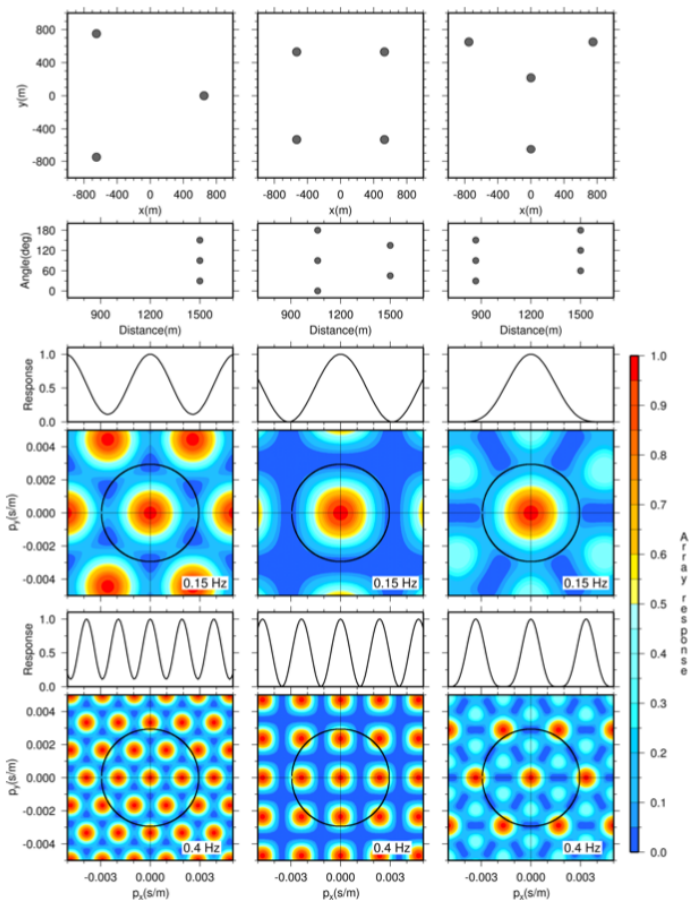

Figure 2.4: *Array layouts with corresponding response patterns. (adopted from Evers, 2008)*
In the middle and right column the side lobes have moved away from the main lobe compared to the left column due to the increase in the number of inter-station distances and angles.
Within this figure $\vec{u_x}$ and $\vec{u_y}$ are replaced by $\vec{p_x}$ and $\vec{p_y}$. The black circle in response patterns represents a v_{app} of 340 m/s, and the cross section right above the pattern shows the response at $p_y = 0$.

2.5 Beamforming

An important application of seismic arrays is the ability to separate coherent signals and noise. Beamforming is a method where the coherent signals are separated from the incoherent signals. In short, the principle of beamforming is to shift the arrival times of the different signals so that the coherent signals will be aligned (Verdon, Kendall, Hicks, & Hill, 2017). Figure 2.5 shows an example of a seismogram that is summed without a time shift of the signals (plain sum) and a seismogram where beamforming is applied (delay and sum).

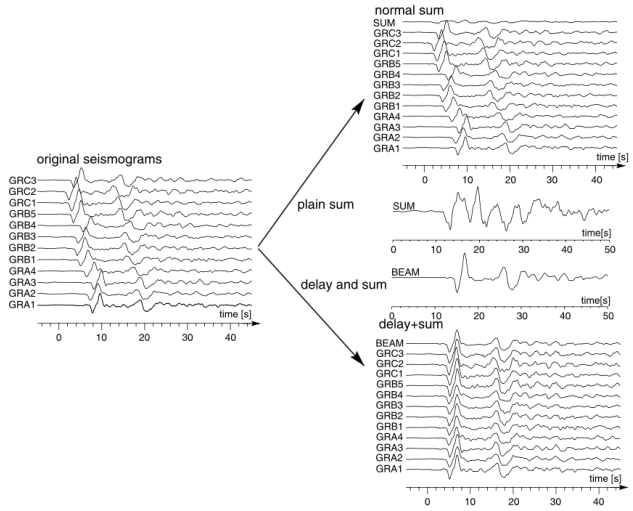

Figure 2.5: *Example of a plain sum and 'delay and sum' (Adopted from Rost & Thomas, 2002)*

Concept of beamforming

Beamforming uses the differential travel times of the plane wavefront as a result of the specific slowness and back azimuth of individual array stations. The beamforming method requires a discrete slowness and back azimuth combination. Based on the area of interest, the slowness vector of the coherent signal is determined and will result in a specific back azimuth.

If the recordings of every single station in the array are correctly shifted in time for a specific slowness and back azimuth, the signals with matching slowness and back azimuth will sum constructively whereas the incoherent signals will interfere destructively. Beamforming will then result in an improvement of the signal-to-noise ratio (SNR), such that the low amplitude signals are detected even where no clear arrival is visible or pick-able on individual traces (Verdon et al., 2017).
When signals are corrected with incorrect values for slowness and back azimuth, it will result in lower signal amplitudes and signal distortion (Rost & Thomas, 2002).

Beamforming formulae

With a given reference location, the location of the i'th array element is given as r_i. The reference location is either the central instrument or the geographic centre of the array (Rost & Thomas, 2002).

When the slowness vector is defined, the time shift can be calculated by Equation 2.17, using a dot product (Arrowsmith, 2021).

$$\tau_i = \vec{r_i} \cdot \vec{u_i} = x_i u_x + y_i u_y \tag{2.17}$$

Where x_i and y_i are the x and y location of station $\vec{r_i}$. After deriving the time shift, τ_i, for each station by solving Equation 2.17, the "delay and sum" process can be defined to calculate the array beam.

If the observation at the i'th array element is written as $x_i(t)$, the beam of the whole array for the slowness

vector, $\vec{u}$, is given by Equation 2.18.

$$\vec{x}(t) = \frac{1}{N}\sum_{i=1}^{N} x_i(t+\tau_i) = \frac{1}{N}\sum_{i=1}^{N} x_i(t+\vec{r_i}\cdot\vec{u}) \tag{2.18}$$

Where N refers to the number of components in the array.

Applying beamforming, the seismic array will act as a wave number filter. The noise reduction depends on the number of stations used in the array processing. Assuming that the signals are perfectly correlated and the noise perfectly uncorrelated, the SNR will be improved by a factor $\sqrt{N}$. The SNR improvement is called array gain, G. The array gain of a sensor array containing N elements can then be written as Equation 2.19 (Schweitzer et al., 2012).

$$G = \sqrt{N} \tag{2.19}$$

2.6 Frequency-Wave number analysis

When the back azimuth is unknown, it can be estimated from the time shifts of the signals from all the stations in the array. There are two ways to do this; a time-domain method, as described within the previous section, or a frequency domain method. In this thesis, the focus is on the frequency domain using a frequency-wave number analysis (f-k analysis). Within this method, the time shifts are handled through phase shifts of the different harmonic components of the waveform (Arrowsmith, 2021).

In general f-k analysis is a matter of forming beams with different slowness vectors and comparing the power of the beams, and then finding the apparent velocity - back azimuth combination that gives the highest energy on the beam (Schweitzer et al., 2012).

The f-k analysis is used as a reference tool in array processing for estimating slowness and the power of the beamformed signal for each trial value of slowness, $\vec{u}$. Recall Equation 2.18 where the beamformed signal for a trial value of $\vec{u}$ is calculated. Thus, the power in a time window with N_T samples performed in the frequency domain, over a frequency band where $f_1 \leq f \leq f_2$ is derived in Equation 2.20, where the normalization factor of $\frac{1}{N_T^2}$ follows form Parseval's theorem (Arrowsmith, 2021).

$$P(u_x, u_y) = \frac{1}{N_T^2}\sum_{f=f_1}^{f_2}\left|\frac{1}{N}\sum_{i=1}^{N} X_i(f)e^{-i2\pi f\vec{r_i}\vec{u}}\right|^2 \tag{2.20}$$

Where $X_i(f)$ is the Fourier transform of the time-shifted recordings $x(t)$ located at the i'th element of the array (Equation 2.3 and Equation 2.4). $X_i(f)$ contains information about the signal's amplitude and time shift, and $e^{-i2\pi f\vec{r_i}\vec{u}}$ is related to the array response, and thus the array resolution (Evers, 2008).

2.7 Fisher statistics

Based upon the f-k spectra, the fisher statistics is derived. Where the f-k analysis includes both signal and noise, the fisher statistics measure the relationship between the signal and noise, also known as the SNR power ratio. The Fisher detector analyzes variances within measurements and is based on the work described by Fisher. Melton

and Bailey have introduced the fisher statistics, the Fisher-ratio, in combination with signal processing (Evers, 2008).
Using an F-ratio, a correlation will be made between the received parameters, the back azimuth and the apparent velocity. Fisher will not only look at the f-k power from these parameters but also focus on the f-k power versus the entire spectrum.
This is done by applying a hypothesis. The hypothesis to be tested H_0 is that all recordings made by the array elements consist of uncorrelated noise. The alternative hypothesis H_1 is valid for the case that not only noise is present but also signal. Evaluated are the variance of the noise σ^2 and the variance σ_α^2, which can not be attributed to the noise since it is common to all signals (Evers, 2008). There are then four effects of the decisions made in the statistical test based on the F-ratio, with two errors:

- When the decision is to reject H_0 while H_0 is true, a type 1 error is made. This results in a '*false alarm*' since the recordings consists of noise.
- When the decision is made to reject H_0 while H_0 was false, a type 2 error is made. Within this situation one is dealing with a missed event in which a coherent infrasonic wave traveled over the array but was not detected.

(Evers, 2008)

	H_0 true	H_0 false H_1 true
Reject H_0	Type 1 error False alarm	No error
Do not reject H_0	No error	Type 2 error Missed event
	$\sigma_\alpha^2 = 0, E(F) = 1$	$\sigma_\alpha^2 > 0, E(F) > 1$

Figure 2.6: *four decisions from the statistical test. H represent the hypothesis, $E(F)$ the expected value of the F-ratio and σ_α^2 the variance (Adopted from Evers, 2008)*

A common approach to calculate the power of the signal is to normalize the power to the ambient power from all other directions-of-arrival. This can be computed from the 'semblance', Equation 2.21 (Arrowsmith, 2021).

$$S = \frac{\sum_{t=t_1}^{t_1+\Delta t} \vec{x}(t)^2}{N \sum_{i=1}^{N} \sum_{t=t_1}^{t_1+\Delta t} x_i(t)^2} \tag{2.21}$$

Where $\vec{x}(t)$ is the beam. The semblance can then be used to derive the F-ratio, Equation2.22 (Arrowsmith, 2021).

$$F = (N-1)\frac{S}{1-S} \tag{2.22}$$

CHAPTER 3

Case study; Nature's Heat geothermal reservoir at Kwintheul

For monitoring the seismic activity of Nature's Heat project, a temporary passive seismic network was installed in Kwintsheul, Netherlands. This network was installed and maintained between July and November 2019, which implies a total recording time of 4 months. The seismic network consisted of 30 three-component short-period seismic sensors, which sampled the wave field at 250 samples per second (Naranjo et al., 2022).

The seismic network was set up in two different geometries. The first geometry consists of two crossing lines, each consisting of 13 stations. These stations covered an area of approximately 3.8 km^2 and were placed at an interstation distance of 150 meters. This geometry characterises the local seismicity and will facilitate array-processing techniques. The second geometry forms an outer ring of 4 peripheral stations, covering an area of approximately 18 km^2 around the geothermal doublet's injection point. This geometry increases the azimuthal coverage of the passive seismic network for improved depth resolution of the possible micro seismic events (Naranjo et al., 2022). The seismic network, as well as the geothermal doublet, is depicted in Figure 3.1.

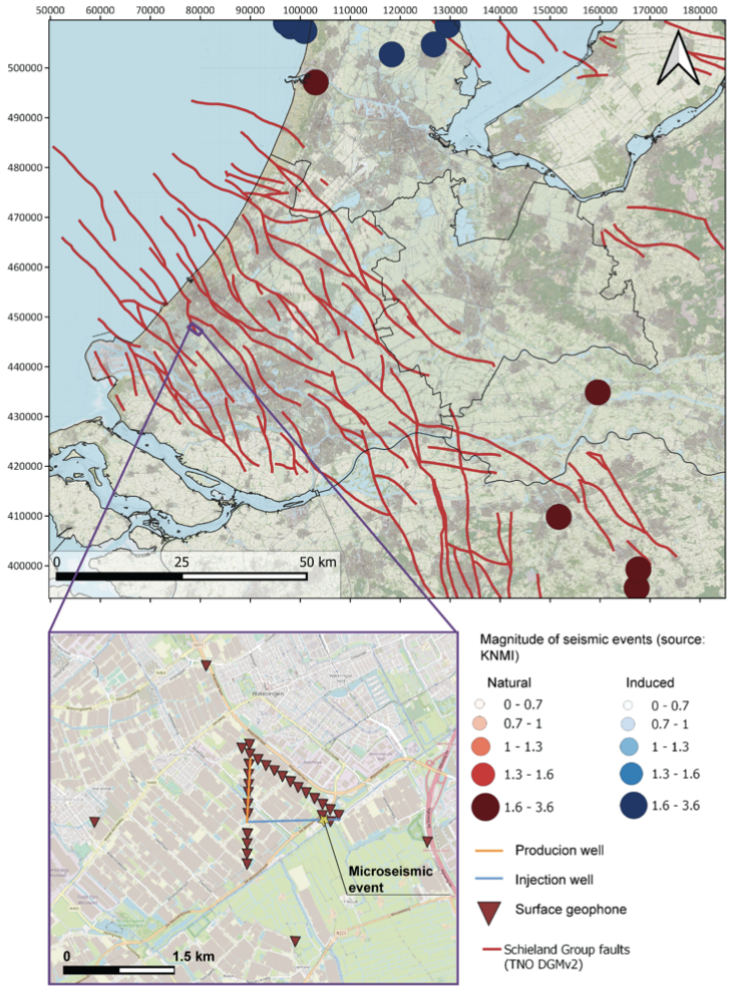

Figure 3.1: *Location of Nature's Heat geothermal operation (the enlarged area), main geological faults of the West Netherlands Basin (WNB), and regional seismicity. (Adopted from Naranjo et al., 2022)*

3.1 Data processing steps

For this thesis, a python code was provided from Remote Online Sessions for Emerging Seismologists (ROSES). This code initially deals with the basic concepts of applying a beamforming algorithm to seismic data. Within the code, one gets familiar with ObsPy, which is a Python toolbox for processing seismological data.
Based on ROSES's code, a beamforming method is applied to the Kwintsheul data. This section will discuss and explain different steps of the process.

3.1.1 Load Kwintsheul data

The first step is to load the metadata of Kwintsheul. There are three different metadata; event metadata, station metadata, and waveform data.

Event metadata

The read events() function opens the event file and will be read into an ObsPy catalogue object. With the help of

this function, the corresponding data/information about the event will be given.

Station metadata

Using read inventory(), a station.xml file can be read and returns an inventory object. The Inventory has a hierarchical structure, consisting of a list of networks, each network containing a list of stations, and each station containing a list of channels. In this case, we are dealing with one network containing 30 stations, each containing three components. However, we are only interested in the vertical component in this thesis. Therefore we select only the Z-component, which results in 30 channels.

Note that the instrument response is included in the station data and, therefore, also in the final results of beamforming. This instrument response can give slightly different results due to error measurements of the sensor. Due to time constraints, the instrument response is not removed.

Waveform data

The seismograms in mseed format will be imported into a stream using the read() function. The stream is a list which contains multiple trace objects. Each trace consists of a data attribute and a stats attribute that contains all metadata information of a trace. Once the waveform data is read, we had to modify the data by detrend all the traces and using a taper to all the traces. In Appendix, figures A.1 to A.6, show the plotted waveform data.

3.1.2 Power Spectral Density Spectrogram

To evaluate the performance of the passive seismic network, it is important to characterise the background seismic noise at each of the stations. As stated in the introduction, the noise can come from natural earth vibrations, cultural sources and instrumental glitches (Naranjo et al., 2022). To quantify this seismic background noise a computation of power spectral densities (PSD) spectrogram is made. The PSD are given in percentages by taking the maximum frequency as a reference, see Equation 3.1.

$$Pxx_{percentage} = \frac{Pxx}{Pxx_{max}} * 100 \tag{3.1}$$

The spectrograms are computed using the function 'signal.sectrogram()', which will form successive Fourier transforms over the data. A Fast Fourier Transform (FFT) is applied within this command to reduce the computing time and complexity of large DFT transforms. A FFT is in principle the same as a DFT, but is more efficiently and much faster than a DFT (Khillar, 2021).

The computed PSD sepctrograms of certain elements from the array are shown in figure 3.2. Appendix figures B.1 to B.4 shows all the PSD spectrograms per element in the array. Some PSD spectrograms showed remarkable features. As is the case within figure 3.2 (a, b, e), where only one point in time indicates a distribution of spectral frequencies, the incoming P-wave. So, in these spectrograms, the incoming S-wave is missing.

Another feature observed was in figure 3.2 (f), where a PSD of KW.029 is shown. This element is located within the second geometry of the seismic network. Within this spectrogram, both the distribution of the P-wave and S-wave can be observed, but with a delay in arrival time of the S-wave. This delay can be observed in all stations of the second geometry. (See Appendix figure B.4, spectrograms KW027, KW028 and KW030).

And figure 3.2 (c and d) shows two examples of stations KW016 and KW018 where noise is observed within the PSD spectrogram. In this case, the noise dominates the signal.

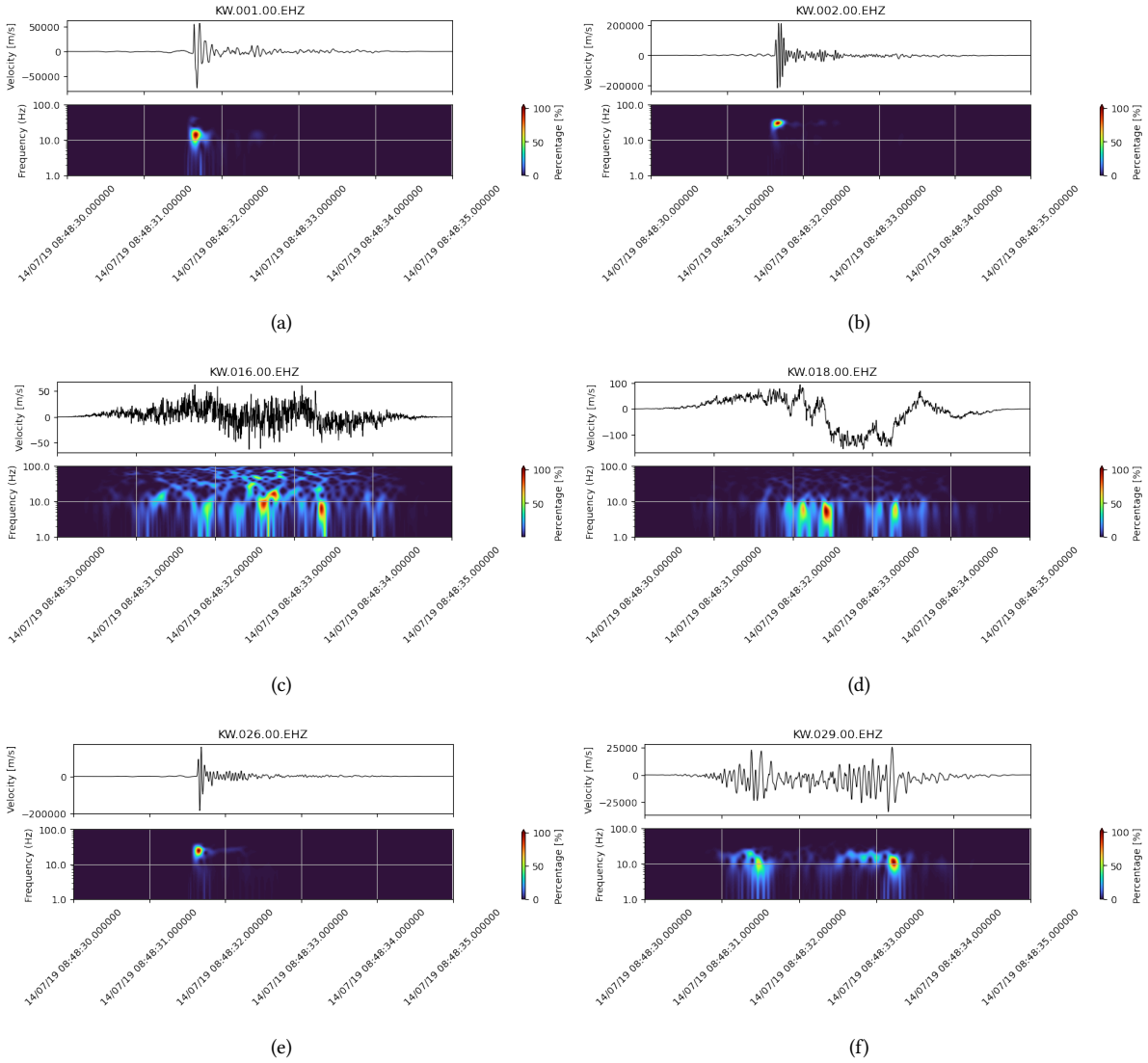

Figure 3.2: *Power spectral density spectrograms.*
KW001, KW002 and KW026 present only a incoming P-wave. KW016 and KW018 present ambient seismic noise. And KW029 present a PSD located in second geometry of the array.

Based on the results of the PSD spectrogram of all elements in the array, a spectral analysis is done. From this, the frequency range of interest was determined to be between 10 Hz and 30 Hz. Therefore, a band pass filter of 10 to 30 Hz is applied for further study.

3.1.3 Array layout and response

Figure 3.1 shows the initial array layout of the Kwintheul array. However, since the seismic event was detected near the array, a near-field-far-field analysis needed to be performed before concluding the array layout and response. Assuming an element is situated in the far-field, the wavefield can be represented as planar wave-

fronts. Nonetheless, when the element is within the near-field of the wavefront, this assumption can not hold. The wavefront propagates spherically within the near-field, and thus the beamforming algorithms need to be transformed to complement these propagation patterns (Benedikt, 2018). The rule of thumb for an array situated in the far-field is $r >> 2\lambda$, where λ is the wavelength.
The wavelength λ of a waveform with constant speed v_{eff} is calculated by Equation 3.2

$$\lambda = \frac{v_{eff}}{f} \tag{3.2}$$

The minimum and maximum velocity are determined from the velocity model of Kwintsheul, shown in 3.4. Within this model, the velocity values range from 1.78km/s to 3.27km/s. After the spectral analysis of section 3.1.2 and figures in appendix B, the frequency range of interest was determined to be 10 to 30 Hz.
Using these parameters in Equation 3.2, the minimum range, within the horizontal plane, between event and array elements is $163.5m$. This has been determined for a velocity of $1.78km/s$ and a frequency of $10Hz$ (the minimum values of the parameters of interest). Changing these parameters into $v_{max} = 3.27km/s$ and $f_{max} = 30Hz$ (the maximum values) the near-field-far-field boundary is at $356m$.

Since the event's location is known, the distances between the event and all the other elements could have been calculated. Based on the boundary condition made previously, elements are highlighted as 'near-field elements' or 'far-field elements'. In addition to the near- and far-field analysis, elements 16 and 18 are removed since these contain a high level of ambient noise. Furthermore, the elements within the second geometry are removed because the array response contained a lot of side lobes (**??**.

As discussed in Section 3.1.3, the array response is a method to identify the resolution of the beamforming. Figure 3.3 shows the array response of all elements in the array layout (a) and an array response of only the selected elements (b). A main lobe (centre lobe) and side-lobes are visible in both array responses. It stands out that the side-lobes are two crossing lines, which is due to the first-array geometry. In appendix figure C.2, an array response is shown of both cross lines of the first array geometry. Within these array responses, you see the origin of the vertical and diagonal side-lobe.
Figure 3.3 (a) shows a better array response compared to (b) because it has a sharper main-lobe and less dominant side-lobes. However, as described before, only the selected elements are used. Therefore, the resolution of the beamforming will be less and have more side-lobes.

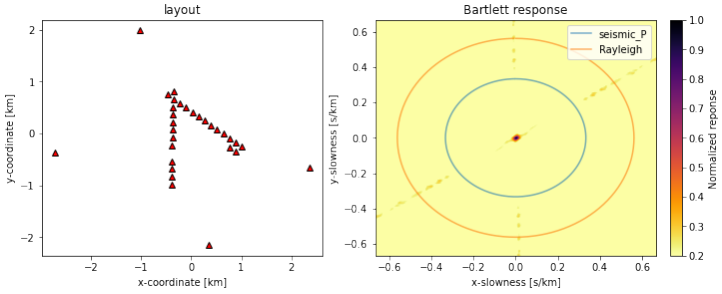

(a)

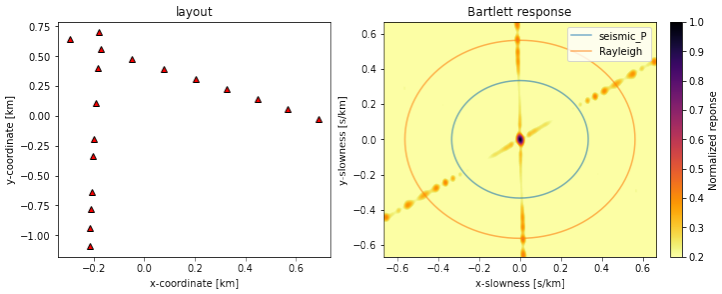

(b)

Figure 3.3: *Array response of Kwintsheul. (a) Array response of all the elements in the array layout (b) array response of the selected far-field situated elements*

3.1.4 Beamforming

From the spectral analysis, the frequency band of interest is defined as 10 to 30 Hz. To apply the beamforming technique, more parameters need to be defined. In this section, first, the beamforming parameters will be discussed, and afterwards, the beamforming results will be displayed.

Beamforming parameters

Within the beamforming technique, a sliding-window method is used. This method will improve the detection of signals or will explore the evolution of the back azimuth of a signal with time (Arrowsmith, 2021). To apply the beamforming algorithm, three important parameters of the sliding-window method are defined as follows:

- The Window length. With sliding-windowing, a small part of the time will be analysed and translated into a frequency. The origin of the signal will be detected within the window.
  The window length is the amount of time that will be analysed when sliding the window. It is preferably set as the length such that the frequency of interest fits. Larger window lengths are applicable for lower frequencies and vice versa. In this case, a window length of 0.4 s is used (Arrowsmith, 2021).

- The overlap parameter. The successive time windows can overlap by some amount to prevent gaps in the data. An overlap will eventually improve the resolution of time-varying effects and signal onset times (Arrowsmith, 2021). The code defines a value of 0.05, meaning an overlap of 95%. The smaller the parameter, the more overlap, which causes more computation time. The overlap in the successive windowing ensures a correlation between the samples and improves the recordings to determine the origin of the

signal.

- Another parameter defined is the Slowness grid. The slowness grid defines the density of the grid and is based on the parameters of interest within the slowness vector: the back azimuth and the apparent velocity. The maximum slowness defines the slowness grid. As mentioned in section 2.3, the medium velocity is the inverse of the medium slowness. From figure 3.4 the velocity values were determined to range between $1.78km/s$ to $3.27km/s$. So for this case study, the minimal velocity out of this range is picked to attain the maximal slowness because then all the signals, P-wave and S-wave, will be taken in consideration. The maximum slowness is computed by taking the inverse of the minimum velocity. So, $1.5km/s$ is taken as the minimum velocity, and therefore $\vec{u} = 0.667s/km$.

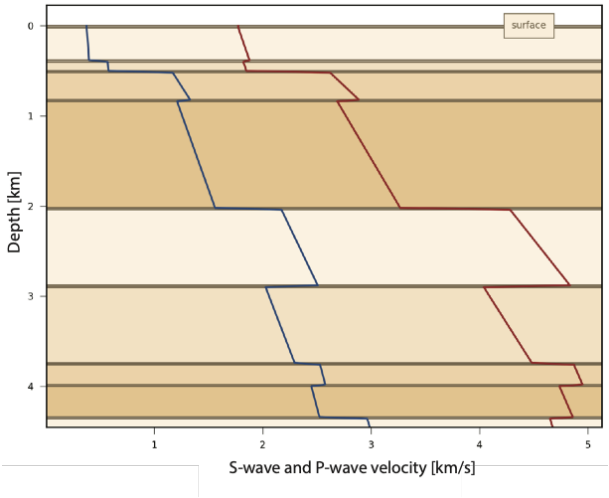

Figure 3.4: *Velocity model of the P-wave and S-wave in Kwintsheul. (Adopted from Naranjo et al., 2022)*

To summarize, the signal detection is achieved by splitting the recordings in 95% overlapping windows, with a window length of 0.4 s. This corresponds, with a sample rate of 250 Hz, to 100 samples per window. Beamforming is performed using a 50x50 rectangular linear slowness grid within the x-y plane. The grid range is from $-0.667s/km$ to $0.667s/km$, which corresponds to a $-1.5km/s$ to $1.5km/s$ velocity. The slowness grid has been chosen, corresponding to the known velocity model of Kwintsheul. The maximal slowness is chosen, to include the S-wave in the results.

Beamforming results

The results of detection and the parameter estimation of the back azimuth and apparent velocity are shown in figure 3.5. The top two frames in figure 3.5 represent the waveform and PSD of element KW022.
The resolved back azimuth, θ, and apparent sound velocity, v_{app}, are estimated to be 300 deg and 6.20 km/s, respectively, as can be determined from the third and fourth frames of figure 3.5.
The maximum F-ratio and f-k power within a window is plotted. Where the F-ratio is calculated with the use of equations 2.21 and 2.22. Two high values of the f-k power trigger a detection according to the F-ratio. The maximum F-ratio is found around 1.5 s, the arriving P-wave, and around 3 s, the arriving S-wave. (see the bottom frame in 3.5).

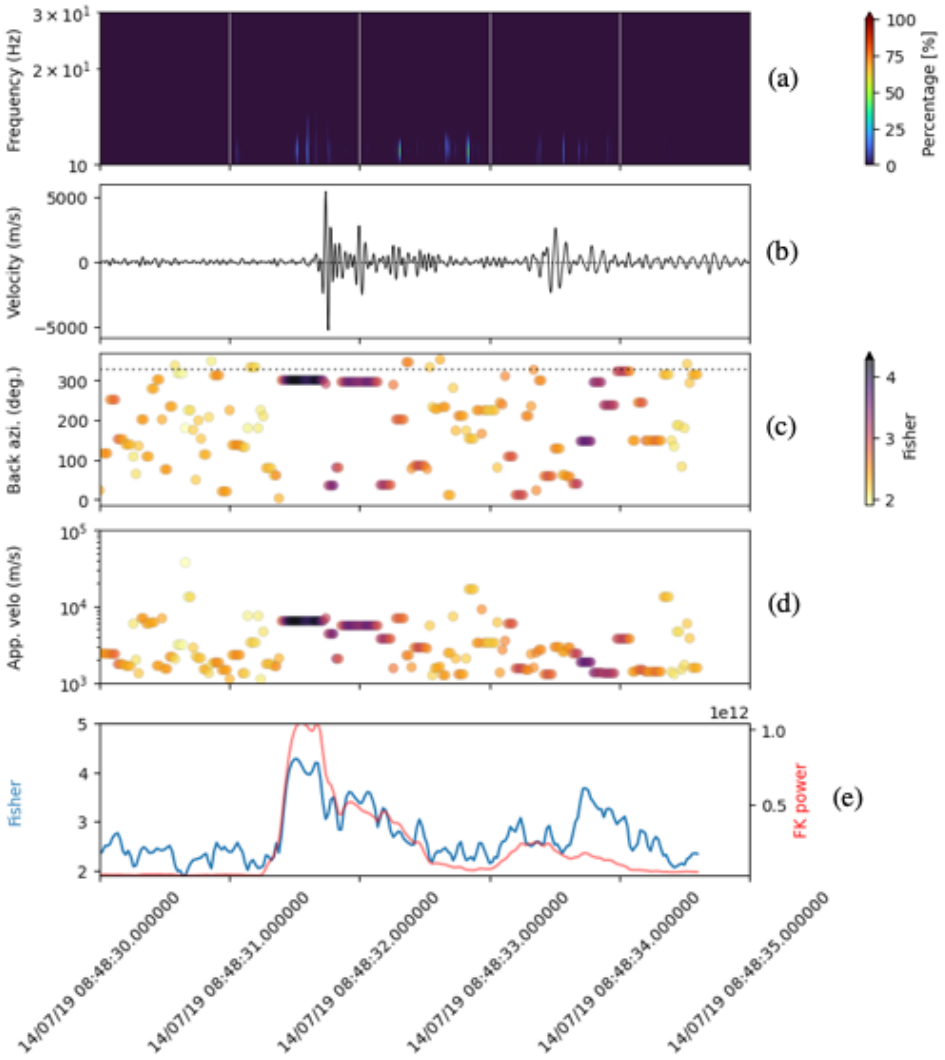

Figure 3.5: *Beamforming with the elements of interest. Taking* $\vec{u} = 1/1.5$
(a) Showing a PSD spectrogram of KW.022 (b) showing the corresponding waveform plot of KW022 (c) the resolved back azimuth (d) the apparent velocity (e) the plotted f-k power and F-ratio

3.1.5 F-k plot

After beamforming, it can be useful to complement the analysis with an f-k analysis that shows a full slowness grid. The f-k analysis is to understand the 'f-k response' that has been computed with the dataset and the chosen set of parameters.

An additional advantage of doing the f-k analysis is that it will also help to understand if any side-lobes exist. From section 3.1.3, some side-lobes were already identified. So, these can be expected to show in the f-k analysis. The computed f-k plots are shown in figures 3.6 and 3.7. Here three results of the f-k analysis are shown. First, the f-k analysis is taken over the whole time period. Secondly, in figure 3.7 (a and b), the f-k analysis is taken over only the time period where the P-wave arrived, and (c and d) show the f-k analysis taken over only the time period where the S-wave arrived.

All three f-k analyses have a frequency range of 10 to 30 Hz. The white cross marks the maximum power, and the colour scale shows the F-ratio, so the coherence of the signal over the array. If a line is drawn from the black cross to the white cross, the angle of this line with respect to the North (clockwise) is the back azimuth, θ. The back azimuth has a value of 300.96 degrees for the incoming P-wave and 315 degrees for the incoming S-wave. These values follow from the slowness grid, $\vec{u_x}$ and $\vec{u_y}$.

The circles in the plot represent the apparent velocity, where the blue circle represent $v_{app} = 6km/s$ and the orange circle represent $v_{app} = 3km/s$. The circles also serve as sort of guidance to estimate the back azimuth visually.

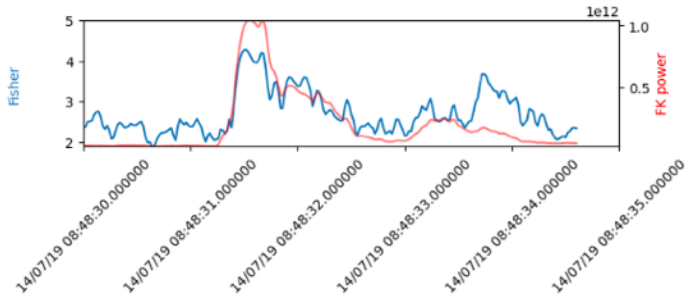

(a)

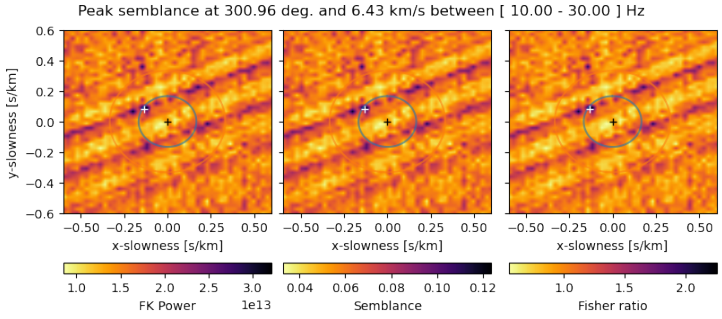

(b)

Figure 3.6: *F-k analysis. (a) Time period of f-k analysis (b) f-k analysis over the whole time period*

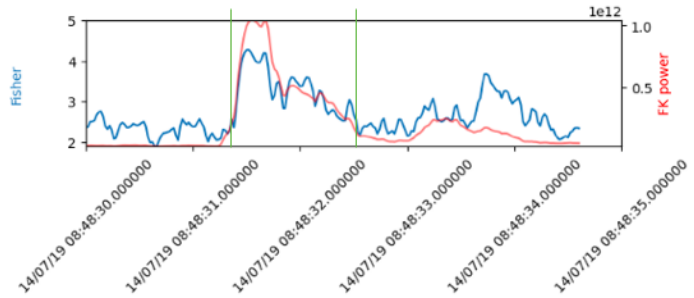

(a)

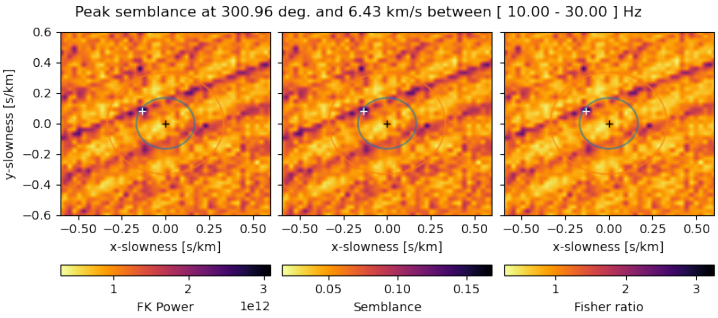

(b)

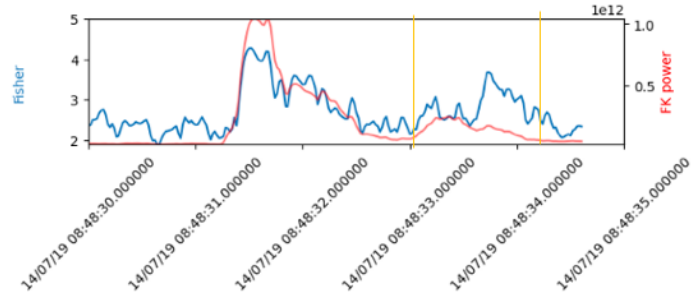

(c)

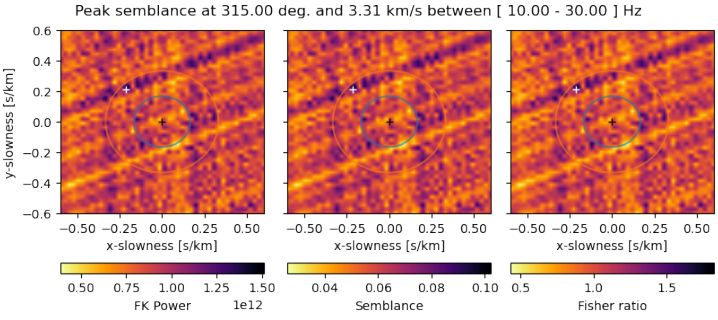

(d)

Figure 3.7: *F-k analysis over P- and S-wave. (a) marked time period of arriving P-wave (b) f-k analysis over only the P-wave (c) marked time period of arriving S-wave (d) f-k analysis over only the S-wave*

CHAPTER 4

Discussion

4.1 Power Spectral Density Spectrogram

Within the previous chapter, section 3.1.2 shows three different features from the power spectral density spectrograms.
The first feature mentioned was from the spectrograms that only showed one point in time that indicates a distribution of spectral frequencies of the incoming P-wave, figure 3.2.a.b.e. This is due to the fact that these stations are located above the origin of the microseismic event. The P-wave propagates in all directions on the ground, while the S-wave needs a surface to propagate. So with a spatial view, an S-wave needs a distance in the x- and y-direction to propagate. When the signal originates directly beneath the array elements, the S-wave has no surface to propagate and, therefore, will not arrive at these elements.

Secondly, in figure 3.2.f, the PSD spectrogram showed a delay in the arrival time of the S-wave. This is because the station, KW.029, is located in the second geometry of the seismic network, which is further away from the source. This causes a delay in arrival time because the longer the distance is to the source, the more time it will take before it arrives.

And finally, in figure 3.2.c. d, the PSD spectrograms showed two spectrograms of stations 16 and 18 where a lot of ambient seismic noise can be observed. After analysing all station's spectrograms, stations 16 and 18 consisted of a lot of background noise and therefore did not display a clear appearance of the incoming P-wave and S-wave. So, in further study, where a beamforming algorithm will be applied, stations 16 and 18 should be neglected to achieve a clean result.

4.2 Beamforming

As beamforming aims to determine the slowness vector and the back azimuth direction, it is important to investigate different slowness values within a range. Additionally, the method requires determining a sliding window with different lengths. After analysing the characteristics of the event and testing different parameters, the following values were selected for applying the beamforming technique:

- A slowness of 0.667 s/km. This parameter is chosen based on the velocity model from Kwintsheul. The velocity from this model was between $1.78km/s$ and the $3.27km/s$. The minimal velocity was chosen to obtain a larger range for the slowness grid. This prevents signals from being excluded from the results.
- A window length of $0.4s$ with an overlapping parameter of 95%.
- A frequency band from 10 to 30 Hz. The frequency band is chosen based on the PSD spectrograms from all elements. After the spectrum analysis, the signals were identified to be between 10 to 30 Hz.

From the beamforming, a back azimuth and apparent velocity for the P-wave and S-wave were achieved, 300.96 deg. & 6.43 km/s and 315 deg. & 3.31 km/s respectively. The computed apparent velocities are higher then the theoretical values from the computed velocity model of Kwintsheul. According to the velocity model, the P-wave should be around a value of 3 km/s, and the S-wave a value around 1.7 km/s. Compared to these values, the apparent velocities of the P- and S-wave are twice as large. This is due to the fact that we are dealing with the horizontal slowness in the xy-plane, which is defined as $\vec{u} = \sqrt{u_x^2 + u_y^2}$. While the actual slowness in the xyz-space is defined as $\vec{u} = \sqrt{u_x^2 + u_y^2 + u_z^2}$. Therefore, to get to the velocity model's effective velocity, a correction must be made with the incident angle using Equation 2.12. When computing Equation 2.12 with the expected effective velocity, the expected incident angle is estimated to be around 51.2 deg ($cos(3/6.43)$). So, the apparent velocity needs to be multiplied by 0.46 to achieve the theoretical velocities of the velocity model.
The resolved back azimuth corresponds to the event regarding the array. In figure 4.1, the orientation of the azimuth of the event's origin and the back azimuth to the elements of the array is shown.

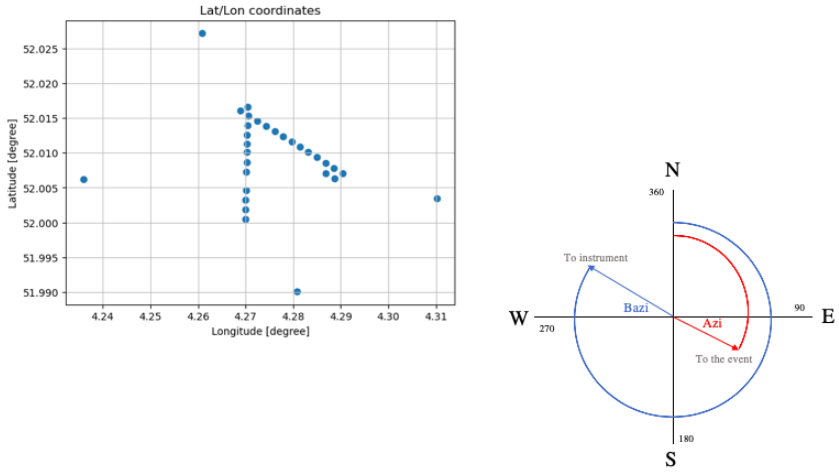

Figure 4.1: *Orientation of the back azimuth and the azimuth of the origin of the event*

4.3 F-k plot

Within the f-k analysis, figures 3.6 and 3.7, side-lobes are observed. This could be because of the use of an incorrect array layout. From section 3.1.3, the array response with the elements used for beamforming already showed side-lobes, which are also visible in the f-k plots. From figure C.2, it could be concluded that the observed side-lobes originated from the crossing lines of elements of the array. To improve the f-k analysis, the array layout needs to be improved by using another array design with only elements situated in the far-field. Also, the array layout was build up without the knowledge of the frequency band that would be received at the element. This could also be a reason why the f-k analysis showed side-lobes. Now that we know at what frequency we are looking, 10-30 Hz, the f-k analysis can be improved to change the array layout to the expected frequency.

4.4 Beamforming for detection

After applying the beamforming technique to the Md 0.16 microseismic event detected in Kwintsheul, it was possible to characterize the back azimuth and apparent velocity of the event's incoming energy. As expected, the estimated back azimuths, corresponding to the signal prior to the event, exhibit scattered values with no visible trend (as shown in Figure 3.5.c). These scattered back azimuth values, with low FK power and low Fischer ratio, show that there are no incoming signals from a source that can be detected by all geophones within the array. It was also shown that when applying the beamforming technique to the microseismic's event time window, the back azimuths converge to the same values. Additionally, during the event's time window, the Fischer ratio and FK power have much higher values. These three features (back azimuth alignments, high Fischer ratios, and high FK power) show that, as expected, there is a coherent signal coming from a specific back azimuth which corresponds to the microseismic event. However, after applying the beamforming approach, the apparent velocity of the measured event did not match with the values of the provided velocity model of Kwintsheul. This was due to the fact that within this study, the beamforming was applied in the xy-plane, horizontal slowness, and not on the xyz-space, actual slowness.
Due to the restriction in the xy plane, the beamforming results in two degrees of freedom. In this case, the apparent velocity and the back azimuth are presented as the two degrees of freedom. However, with respect to the seismic analysis, the incident angle and depth are also interesting to resolve. This can be done in two ways:

- By still using the xy plane, but replacing the apparent velocity for the back azimuth and incident angle. As a result, to achieve more information about the back azimuth and incident angle, there is no information about the apparent and effective velocity. A drawback of generating the slowness grid based on the incident angle and the back azimuth is that the difference between the P- and S-wave can not be determined anymore since these are resolved based on the apparent velocity.

- Or by adding elements to the array in the z-direction by using a borehole. This will result in an xyz-space analysis, with the incident angle as a third-degree of freedom.

For further studies on the Kwintsheul data, this would be interesting to consider.
Contingent on successfully meeting the objective of this thesis; to assess whether beamforming is capable of lowering the detection threshold, and determining the signals incidence angle and azimuth, using data recorded by the Kwintsheul seismic array. Beamforming could be applied to the entire Kwintsheul data set and set a

detection threshold based on the FK power, Fischer ratio and the alignment of the back azimuths to find seismic events that were not detected by the energy-based algorithm.

CHAPTER 5

Conclusion

To monitor the seismic activity around the geothermal field of the Nature's Heat project, a passive seismic network was installed and maintained for four months in Kwintsheul, Netherlands. The network detected one single weak event. The aim of this bachelor thesis was to assess whether beamforming is capable of detecting and estimating the direction of the measured seismic event in the Kwintsheul data. To restate the research question:

Does beamforming lead to an improved detection of the measured microseismic event found in the Kwintsheul data?

To answer this research question, several data processing steps were applied. Spectrum analysis of the received P- and S-wave was done from the PSD spectrogram, followed by the beamforming technique. For the beamforming the following parameters were used; a frequency band-pass filter of 10 to 30 Hz, a window length of $0.4s$ with an overlap parameter of 95%, and a slowness grid of -0.667 x 0.667 s/km, corresponding to the minimal velocity of $-1.5km/s$ to $1.5km/s$. Beamforming resulted in the detection of an event, an estimation of the back azimuth, 300 to 315 deg., and apparent velocity of the P- and S-wave was defined, $6.4km/s$ and $3.3km/s$ respectively. The apparent velocities did not match the theoretical velocities based on the velocity model of Kwintsheul. However, assuming an incident angle of 51.2 deg. the effective velocity becomes $3km/s$, which corresponds to the velocity model. The properties of the fisher statistics and the f-k analysis showed that beamforming can discriminate coherent signals from incoherent signals.

The result is obtained by only using the elements of the array within the far-field of the event. According to the array response, the resolution with the used elements was less compared to the array response with all the elements of the array. This is also observed in the f-k analysis plots, where the side-lobes of the array response are dominantly present. Therefore, the capability of detecting interfering signals relies on the resolution of the beamform, which is quantified by the array response, and dependent on the beamform technique and the array layout.

Contingent on successfully meeting the objective of this thesis, beamforming could be applied to the entire

Kwintsheul dataset to find seismic events that were not detected by the energy-based algorithm. Additionally, it would be interesting to resolve the incident angle and depth, besides the back azimuth and apparent velocity, of the seismic event with respect to the seismic analysis.

References

Arrowsmith, S. (2021). Array and network methods. Retrieved from https://github.com/roseseismo/roses2020/blob/master/unit05/array_processing.pdf

Baig, A., & Urbancic, T. (2010, Feb). *Magnitude determination, event detectability, and assessing the effectiveness of microseismic monitoring programs in petroleum applications.* Retrieved from https://csegrecorder.com/articles/view/magnitude-determination-event-detectability-and-assessing-effectiveness

Benedikt, F. B. (2018). *Infrasound data analysis of signals produced by greenlandic glaciers* (Unpublished doctoral dissertation).

Brophy, P. (1997). Environmental advantages to the utilization of geothermal energy. *Renewable Energy*, *10*(2), 367-377. Retrieved from https://www.sciencedirect.com/science/article/pii/0960148196000948 (World Renewable Energy Congress IV Renewable Energy, Energy Efficiency and the Environment) doi: https://doi.org/10.1016/0960-1481(96)00094-8

Capon, J. (1969). High-resolution frequency-wavenumber spectrum analysis. *Proceedings of the IEEE*, *57*(8), 1408-1418. doi: 10.1109/PROC.1969.7278

Dempster, J. (2001). Chapter six - signal analysis and measurement. In J. Dempster (Ed.), *The laboratory computer* (p. 136-171). London: Academic Press. Retrieved from https://www.sciencedirect.com/science/article/pii/B9780122095511500398 doi: https://doi.org/10.1016/B978-012209551-1/50039-8

Denholm-Price, J. C. W., & Rees, J. M. (1999). Detecting waves using an array of sensors. *Monthly Weather Review*, *127*(1), 57 - 69. Retrieved from https://journals.ametsoc.org/view/journals/mwre/127/1/1520-0493_1999_127_0057_dwuaao_2.0.co_2.xml doi: 10.1175/1520-0493(1999)127⟨0057:DWUAAO⟩2.0.CO;2

EBN, Geothermie, P., Warmtenetwerk, S., & DAGO. (2018). *Master plan geothermal energy in the netherlands* (Tech. Rep.).

Evers, L. (2008). *The inaudible symphony: on the detection and source identification of atmospheric infrasound* (Unpublished doctoral dissertation). Delft University of Technology.

Khillar, S. (2021, Sep). *Difference between fft and dft.* Retrieved from http://www.differencebetween.net/technology/difference-between-fft-and-dft/

Naranjo, D., Draganov, D., Polychronopoulou, K., de Bas, M., & Weemstra, C. (2022). Seismic monitoring of nature's heat geothermal reservoir in kwintsheul (netherlands).

Rost, S., & Thomas, C. (2002). Array seismology: Methods and applications. *Reviews of Geophysics*, *40*(3), 2-1-2-27. Retrieved from https://agupubs.onlinelibrary.wiley.com/doi/abs/10.1029/2000RG000100 doi: https://doi.org/10.1029/2000RG000100

Schweitzer, J., Fyen, J., Mykkeltveit, S., Gibbons, S. J., Pirli, M., Kühn, D., & Kværna, T. (2012). Seismic arrays. *Potsdam : Deutsches GeoForschungsZentrum GFZ*, 1–80. doi: 10.2312/GFZ.NMSOP-2_ch9

Semmlow, J. (2012). Chapter 4 - the fourier transform and power spectrum: Implications and applications. In J. Semmlow (Ed.), *Signals and systems for bioengineers (second edition)* (Second Edition ed., p. 131-165). Boston: Academic Press. Retrieved from https://www.sciencedirect.com/science/article/pii/B9780123849823000043 doi: https://doi.org/10.1016/B978-0-12-384982-3.00004-3

Verdon, J., Kendall, J., Hicks, S., & Hill, P. (2017, November 1). Using beam-forming to maximise the detection capability of small, sparse seismometer arrays deployed to monitor oilfield activities. *Geophysical Prospecting*, *65*(6), 1582–1596. doi: 10.1111/1365-2478.12498

Ziemer, R. E., Tranter, W. H., & Fanning, D. R. (2011). *Signals and systems: Continuous and discrete* (4th ed.). Pearson Education Limited.

APPENDIX A

Waveform data

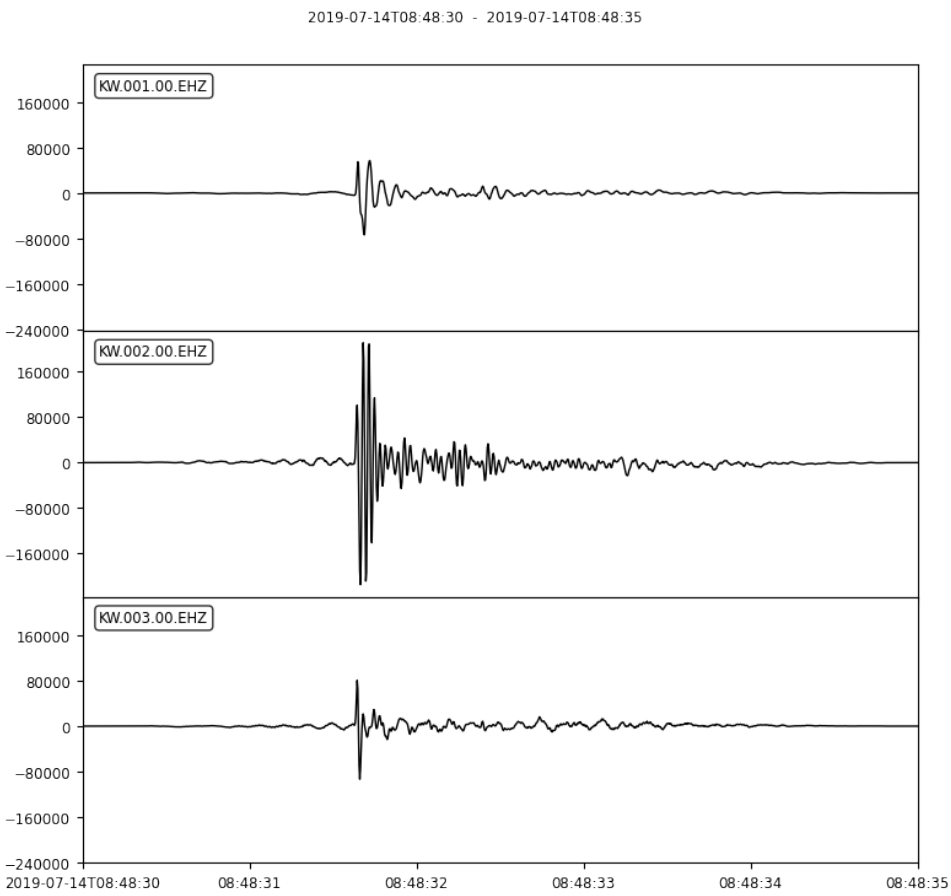

Figure A.1: *Waveform data, traces 1-3*

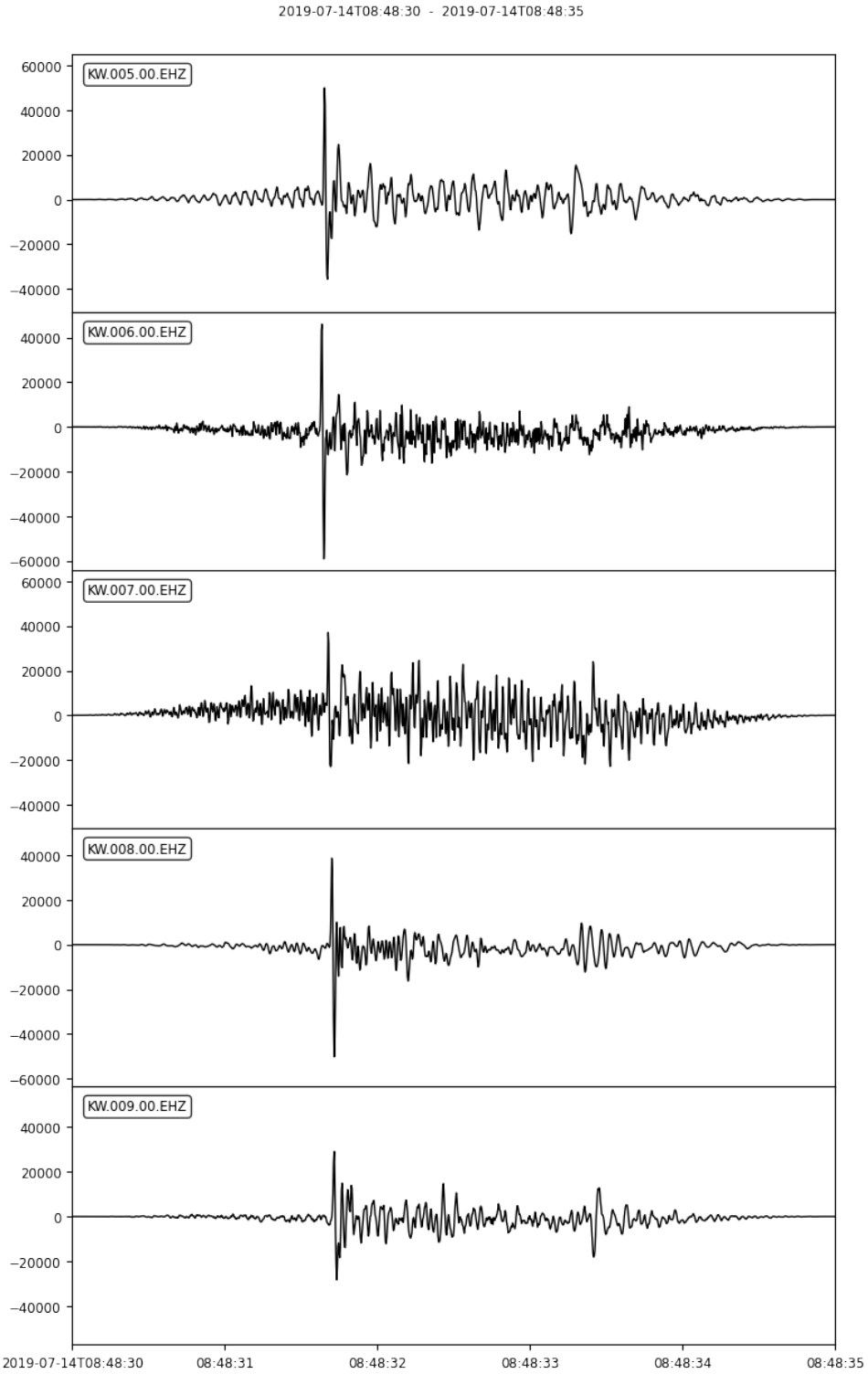

Figure A.2: *Waveform data, traces 5-9*

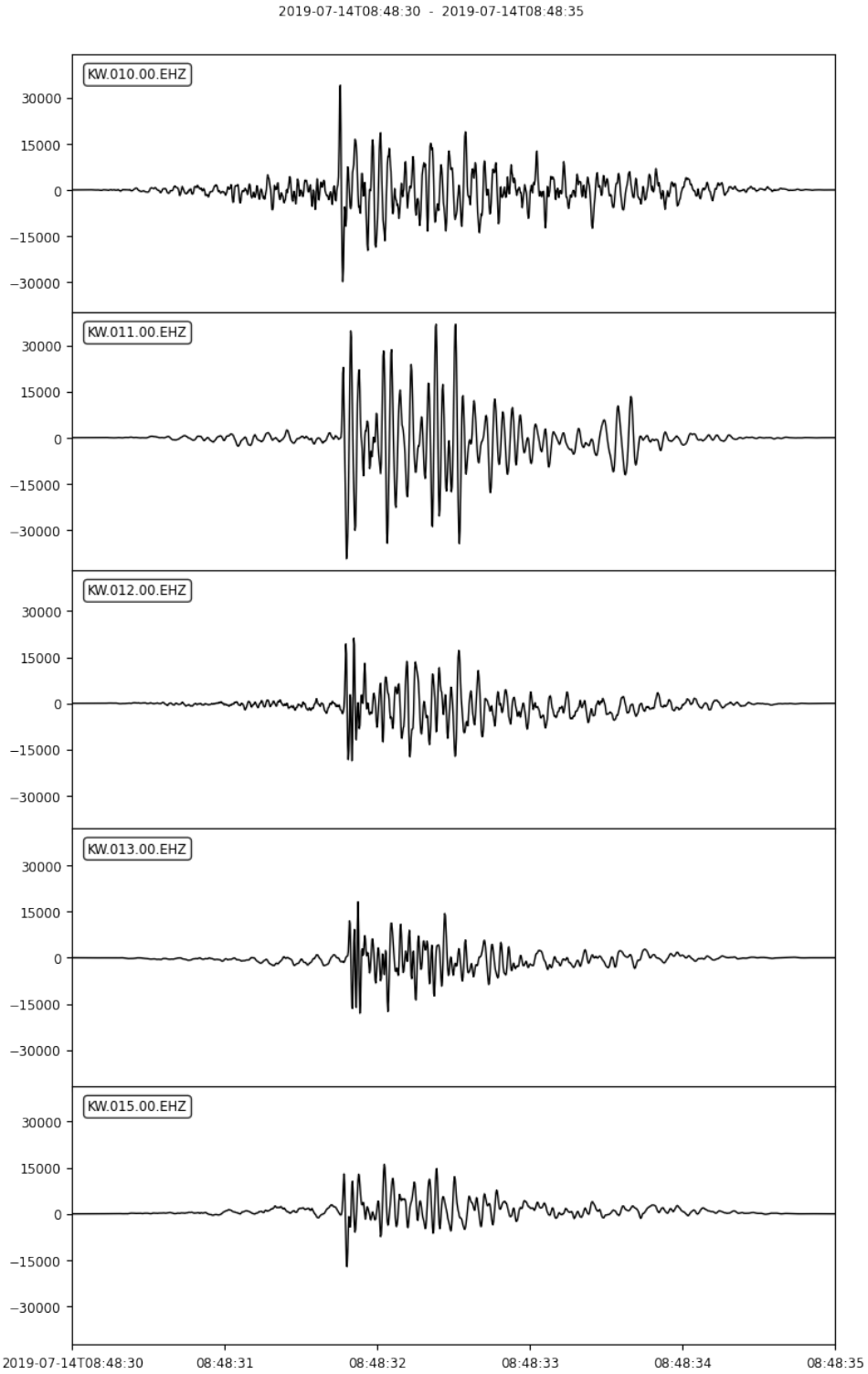

Figure A.3: *Waveform data, traces 10-15*

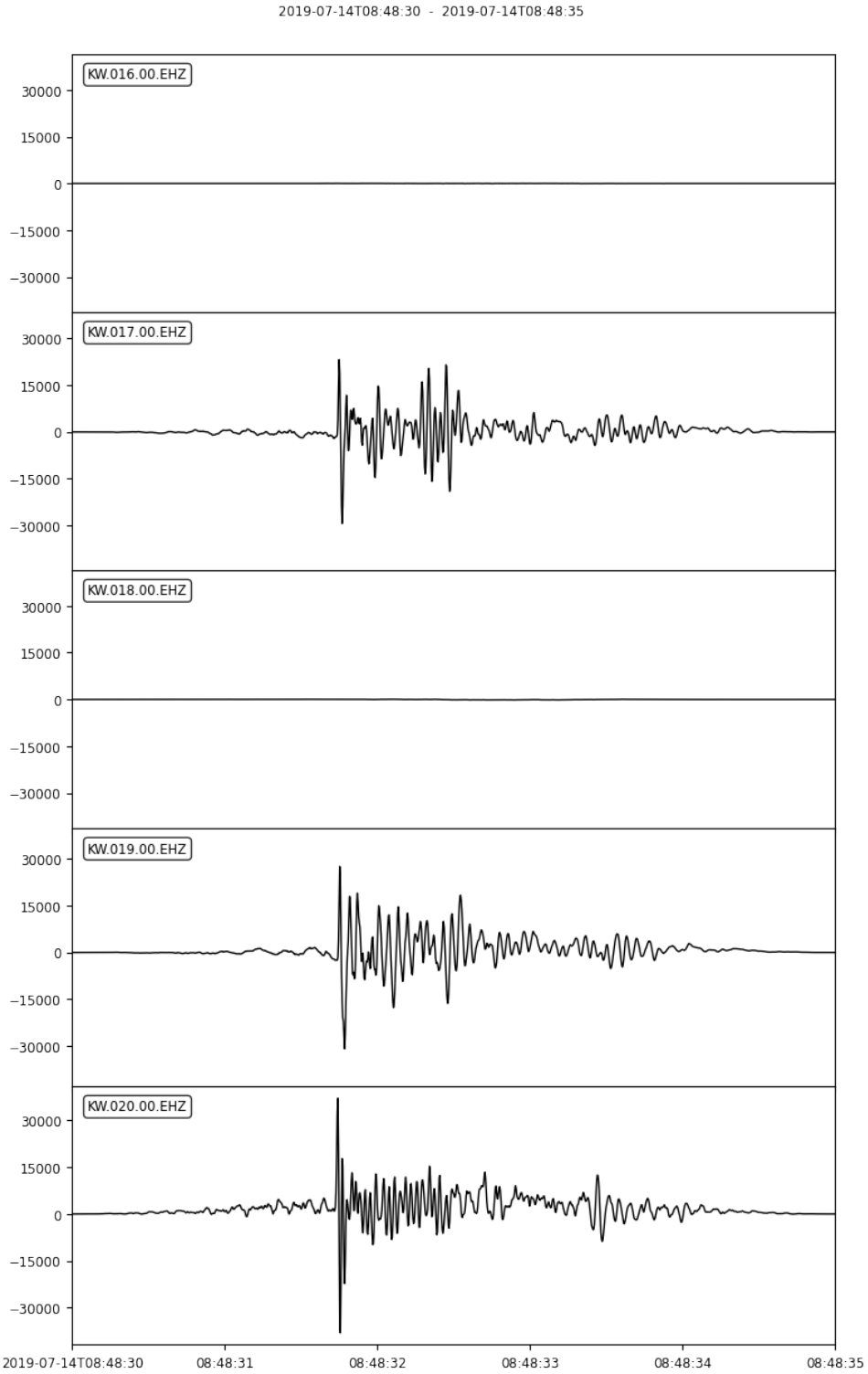

Figure A.4: *Waveform data, traces 16-20*

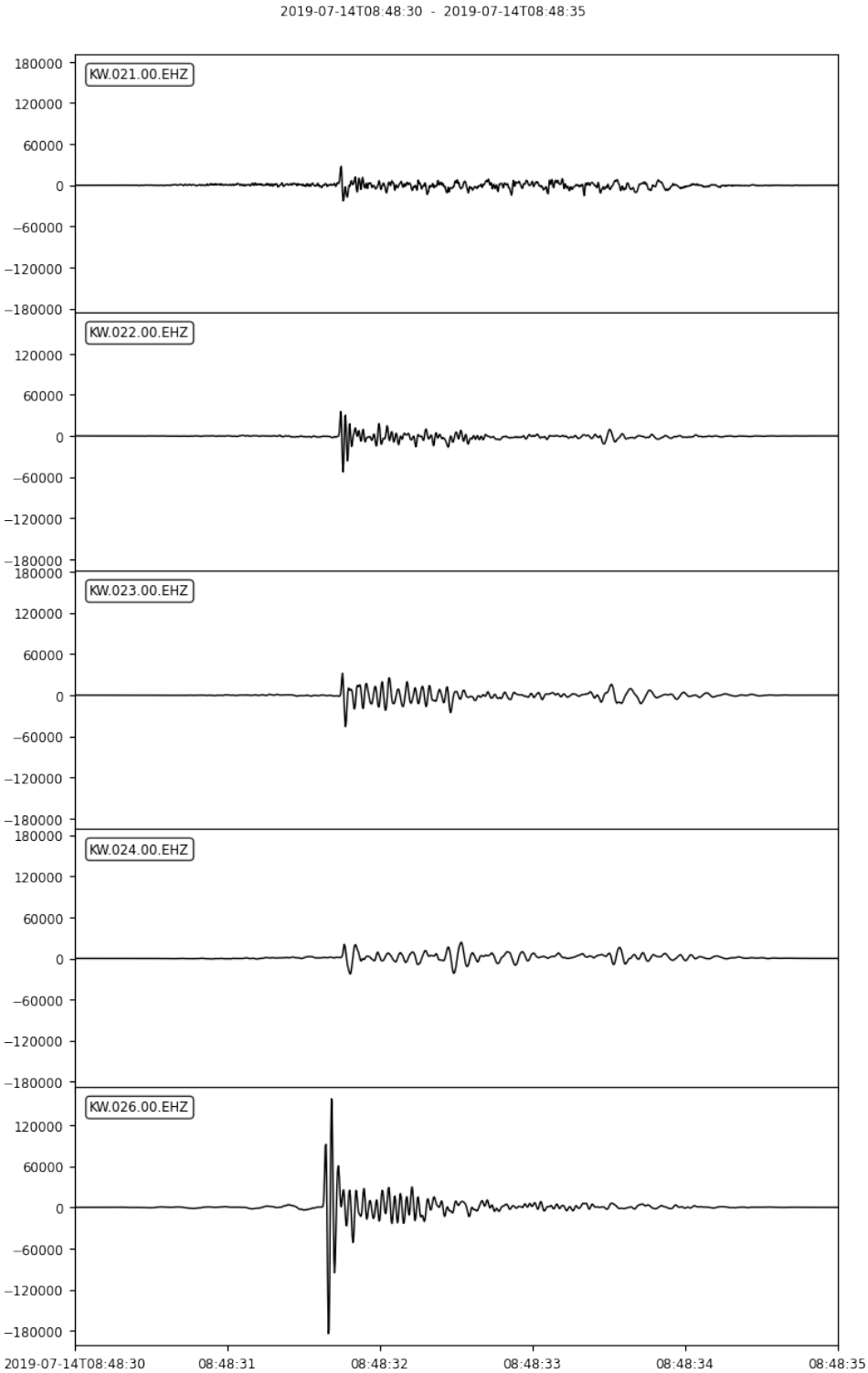

Figure A.5: *Waveform data, traces 21-26*

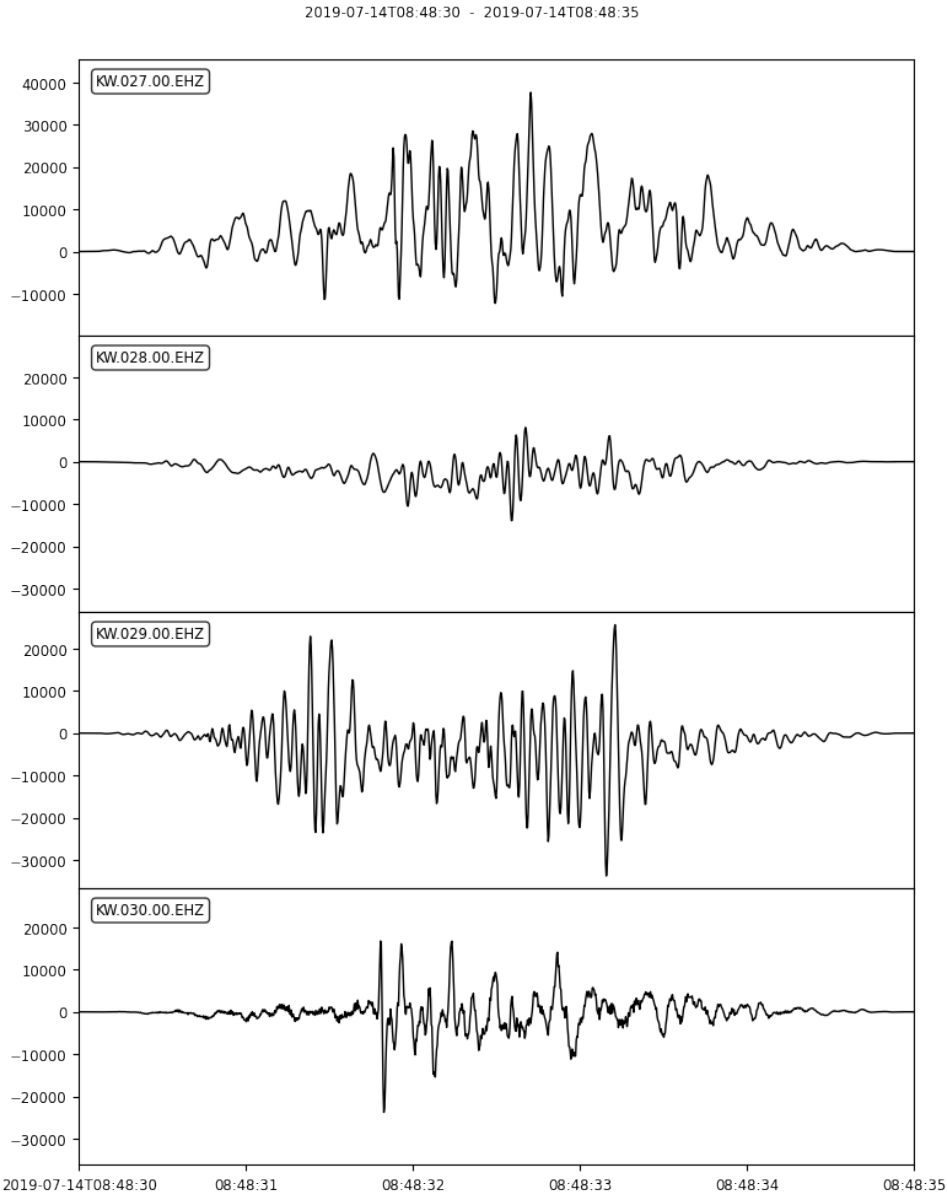

Figure A.6: *Waveform data, traces 27-30*

APPENDIX B

Power spectral density spectrogram

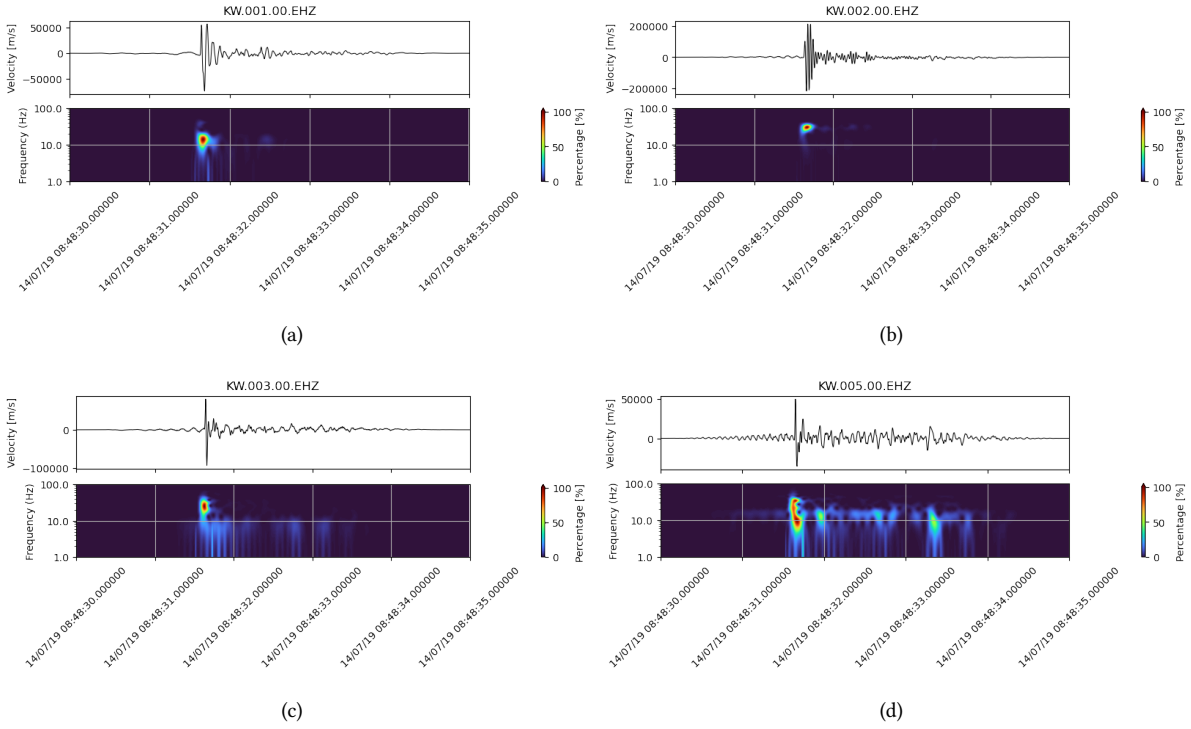

Figure B.1: *Power spectral density (a) station KW.001 (b) station KW.002 (c) station KW.003 (d) station KW.005*

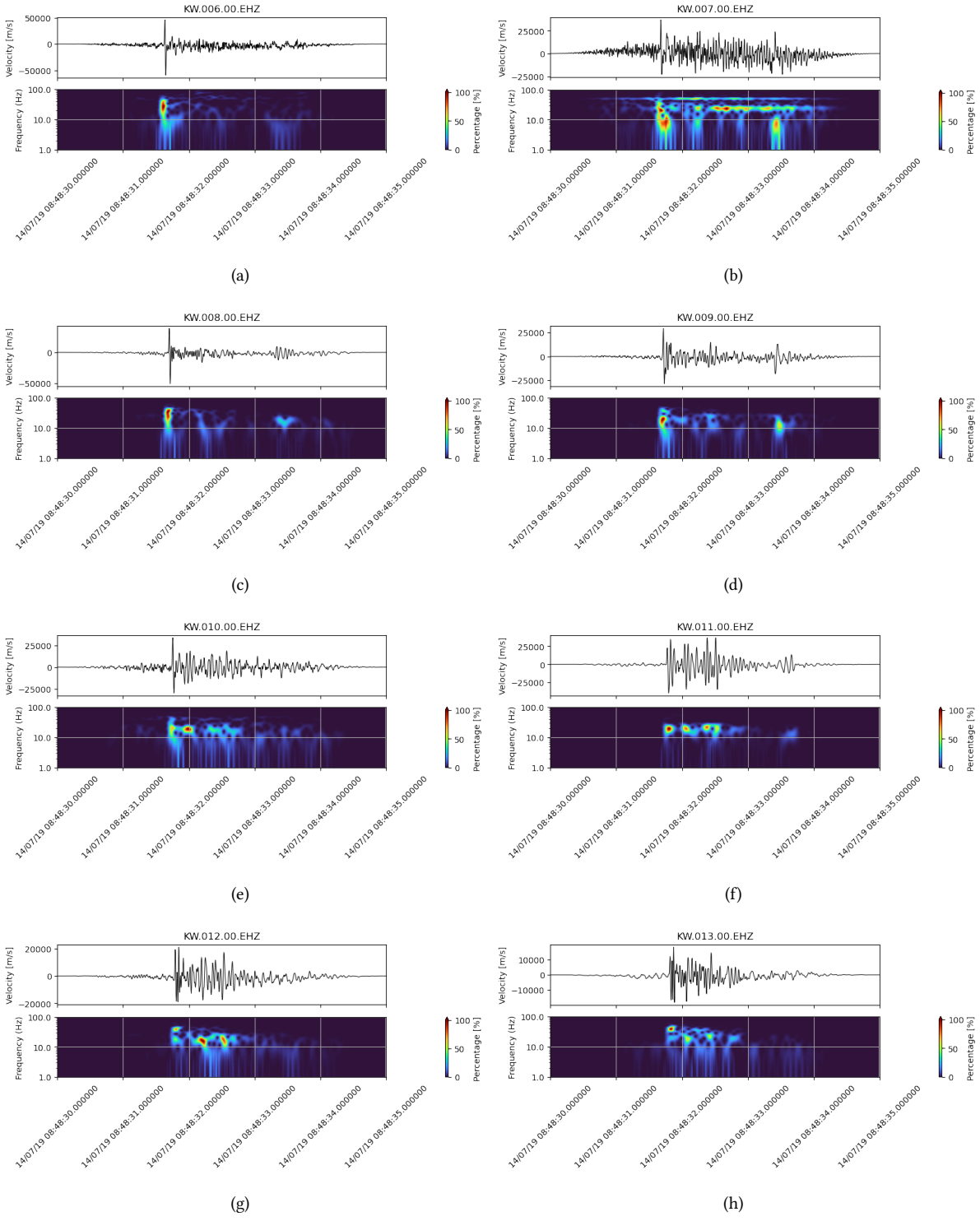

Figure B.2: *Power spectral density (a) station KW.006 (b) station KW.007 (c) station KW.008 (d) station KW.009 (e) station KW.010 (f) station KW.011 (g) station KW.012 (h) station KW.013*

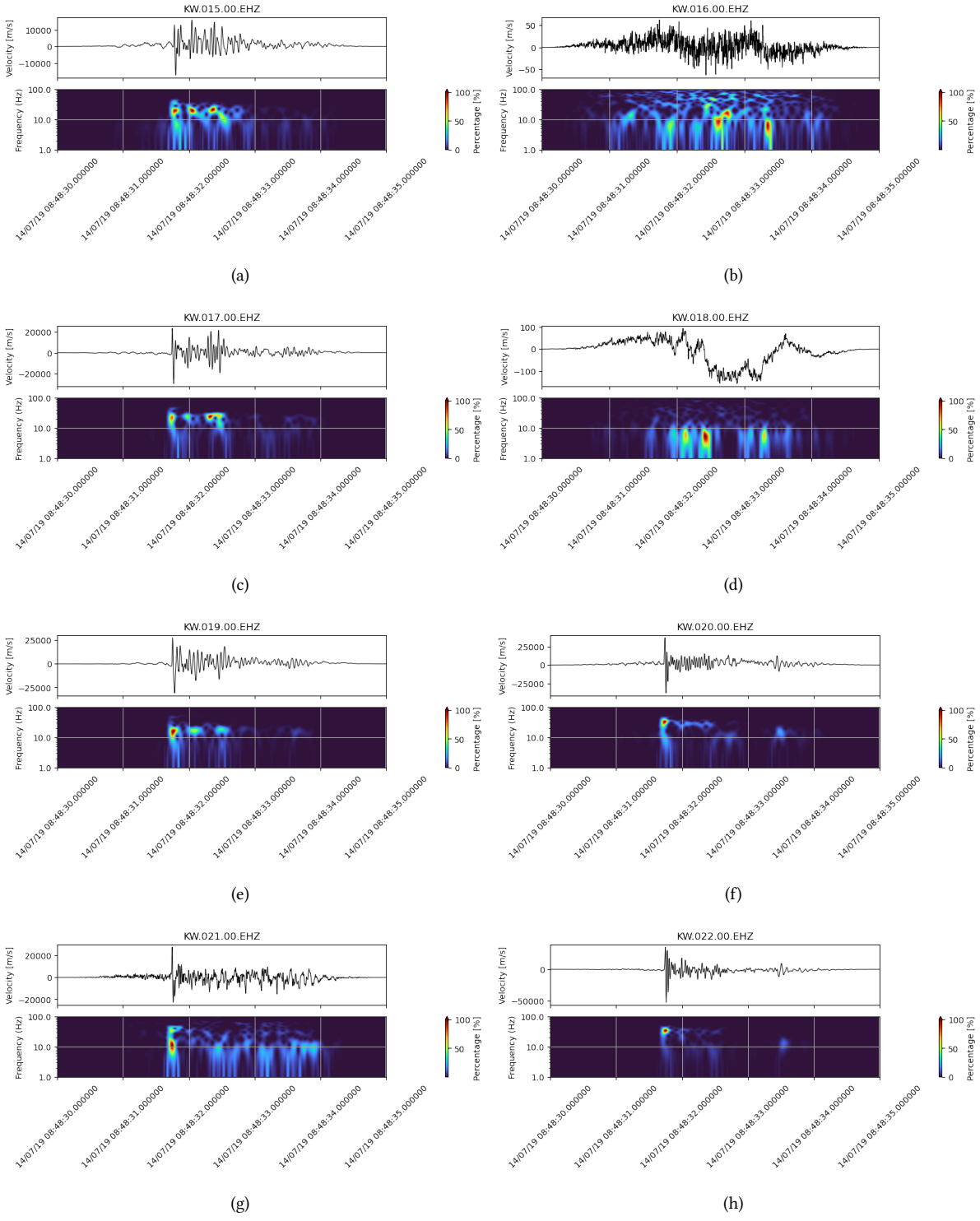

Figure B.3: *Power spectral density (a) station KW.015 (b) station KW.016 (c) station KW.017 (d) station KW.018 (e) station KW.019 (f) station KW.020 (g) station KW.021 (h) station KW.022*

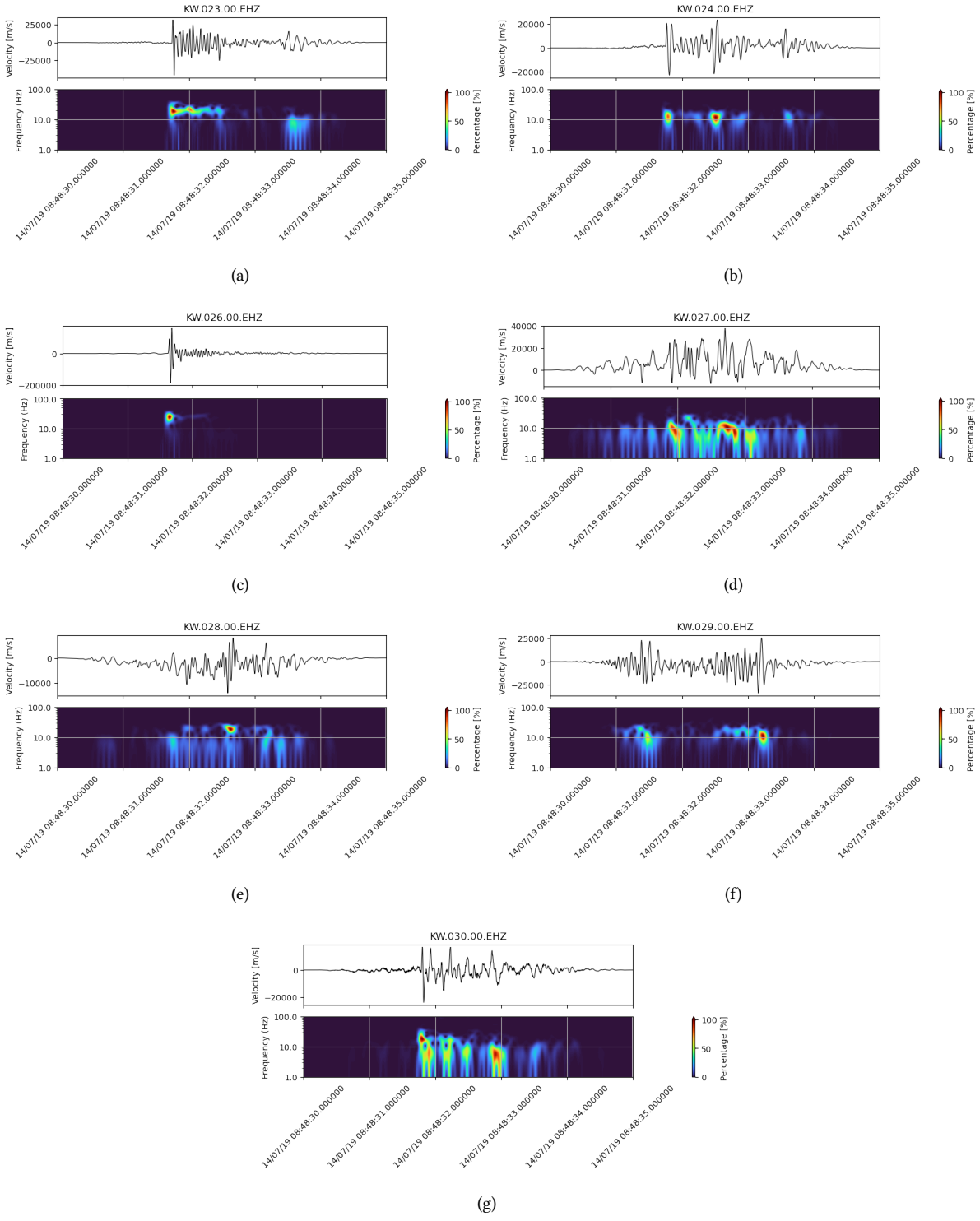

Figure B.4: *Power spectral density (a) station KW.023 (b) station KW.024 (c) station KW.026 (d) station KW.027 (e) station KW.028 (f) station KW.029 (g) station KW.030*

APPENDIX C

Array response

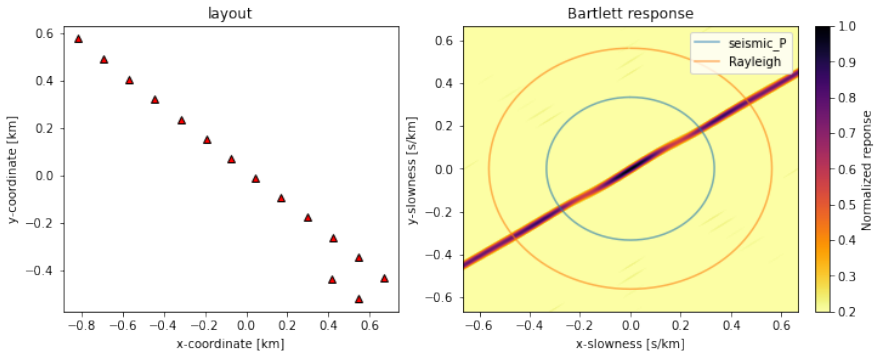

(a)

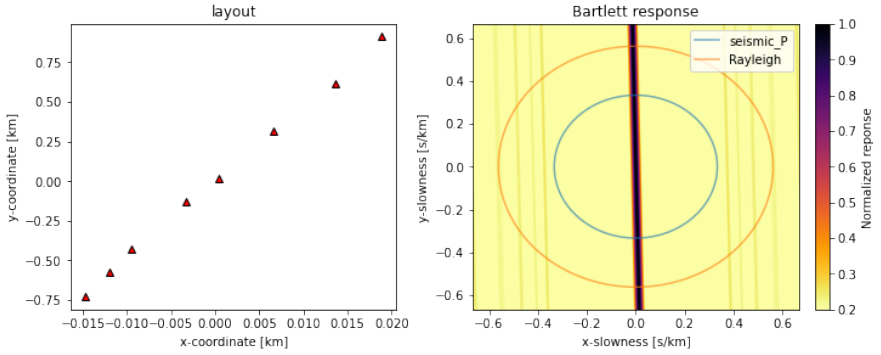

(b)

Figure C.1: *Array response of the first geometry (a) right cross line (b) left cross line*

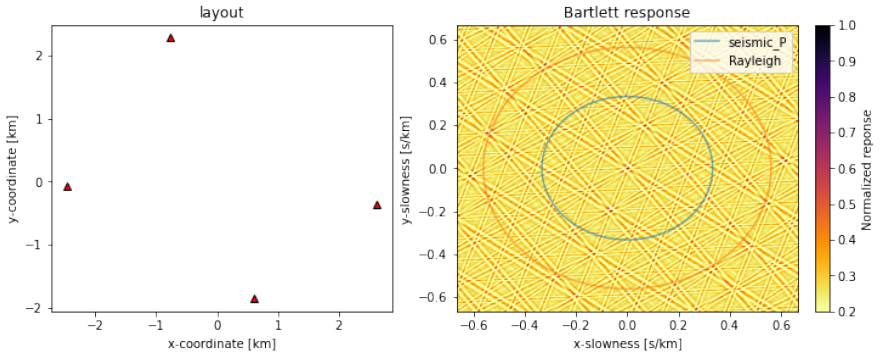

Figure C.2: *Array response of the second array geometry*

APPENDIX D

Beamforming

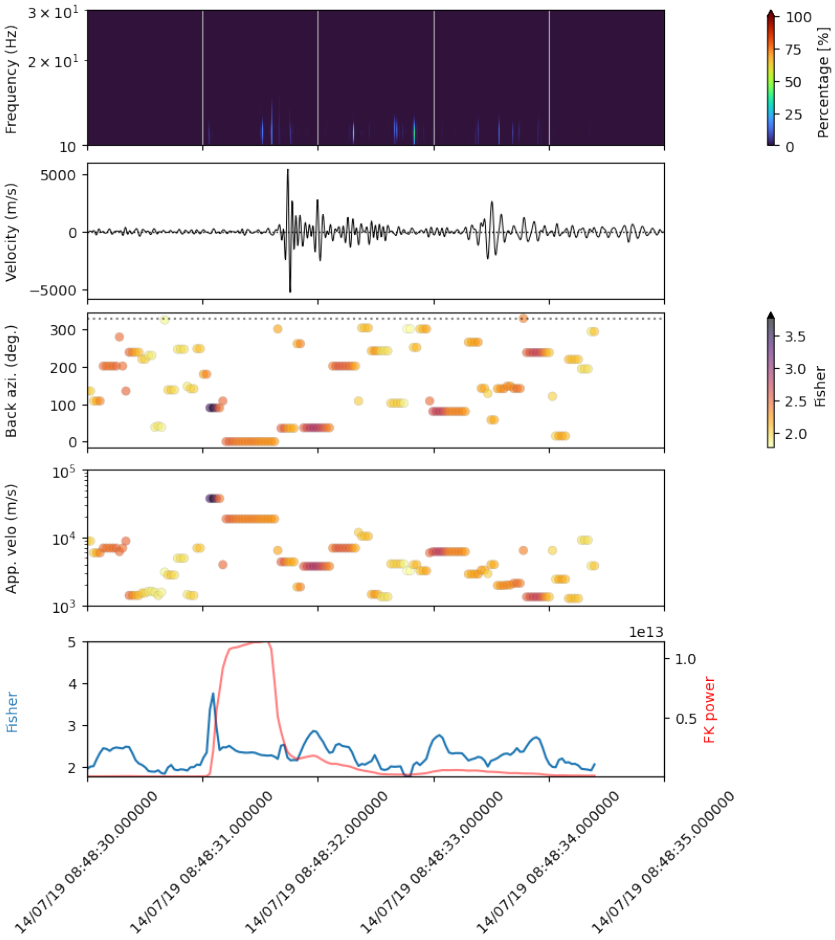

Figure D.1: *Beamforming of all elements in the first array geometry*

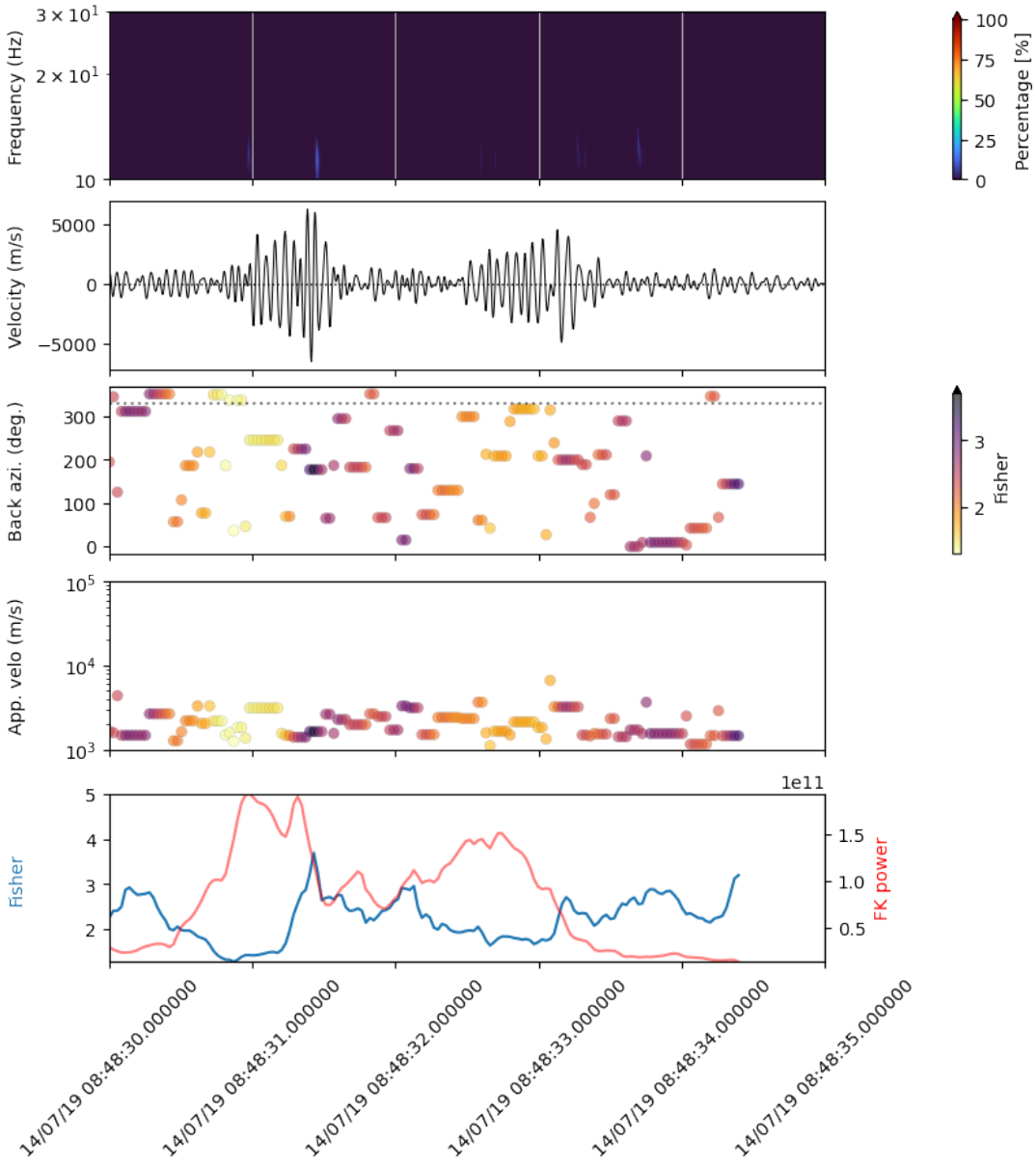

Figure D.2: *Beamforming of all elements in the second array geometry*

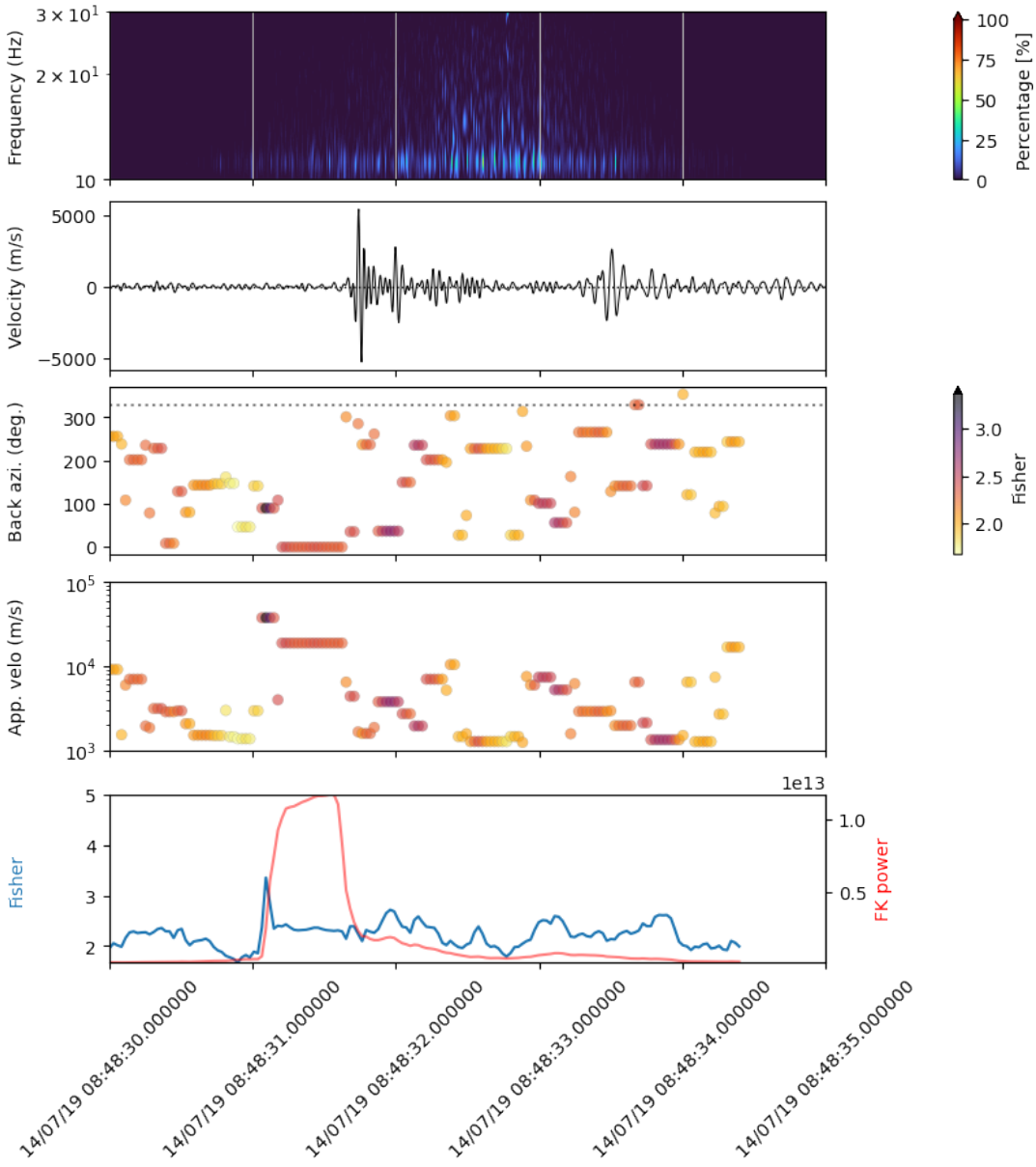

Figure D.3: *Beamforming of all elements in both array geometries*